Anelastic Internal Wave Reflection and Transmission in Uniform Retrograde Shear

by

Lauren E. Eberly

A thesis submitted in partial fulfillment of the requirements for the degree of

Master of Science

Department of Department of Earth and Atmosphere Science
University of Alberta

Abstract

We perform fully nonlinear simulations in two dimensions of a horizontally periodic, vertically localized, anelastic internal wavepacket in order to examine the effects of weak and strong nonlinearity upon wavepackets approaching a reflection level in uniform retrograde shear. Transmission, reflection and momentum deposition are measured in terms of the horizontal momentum associated with the wave-induced mean flow. These are determined in part as they depend upon the initial wavenumber vector, $\vec{k} = (k, m)$, which determines the modulational stability (if $|m/k| \gtrsim 0.7$) or instability (if $|m/k| \lesssim 0.7$) of moderately large amplitude quasi-monochromatic internal wavepackets. Whether modulationally stable or unstable, the evolution of the wavepacket is determined by the height of the reflection level predicted by linear theory, z_r, relative to the height, z_Δ, at which weak nonlinearity becomes significant, and the height, $z_b > z_\Delta$, at which linear theory predicts anelastic waves first overturn in the absence of shear. If $z_r < z_\Delta$, the amplitude remains sufficiently small and the waves reflect as predicted by linear theory. If z_r is moderately larger than z_Δ, a fraction of the momentum associated with the wavepackets transmits past the reflection level. This is because the positive shear associated with the wave-induced mean flow can partially shield the wavepacket from the influence of the negative background shear enhancing its transmission. The effect is enhanced for weakly nonlinear modulationally unstable wavepackets that narrow and grow in amplitude faster than the anelastic growth rate. However, as nonlinear effects become more pronounced, a significant fraction of the momentum associated with the wavepacket is irreversibly deposited to the background below the reflection level. This is particularly the case for modulationally unstable wavepackets, whose enhanced

amplitude growth leads to overturning below the predicted breaking level. Because the growth in the amplitude envelope of modulationally stable wavepackets is retarded by weakly nonlinear effects, reflection is enhanced and transmission retarded relative to their modulationally unstable counterparts. Applications to mountain wave propagation through the stratosphere in the winter hemisphere are discussed as well as applications of a fully nonlinear, anelastic wave model to non-constant buoyancy frequency backgrounds.

Preface

Work related to wave reflection and transmission in uniform shear (not wave tuneling) has been published as L.Eberly, B.R. Sutherland "Anelastic internal wave reflection and transmission in uniform retrograde shear," *Physics of Fluids*, vol. 26, 026601. I was responsible for simulation analysis as well as composition of the manuscript. Bruce R. Sutherland was the supervisory author and was involved with concept formation and manuscript composition.

To Ty who followed me to the frozen North and to Will who is coming back with us.

Acknowledgements

I would like to acknowledge my parents for supporting me in my career decisions - even when it meant moving out of the country. And my husband for his immense support (and especially for finding late-night, genius solutions for everything from printer issues to code problems).

I'd also like to thank my advisor, Bruce Sutherland, for guiding me with this research and providing the opportunity to study here in Edmonton and to the members of our research group who were quick to provide valuable insight.

Contents

List of Tables

List of Figures

Chapter 1

Introduction

One of the most critical mechanisms for transporting momentum vertically in the atmosphere is by internal wave propagation and breaking. The Earth's atmosphere is characterized by having variable density with height due to the temperature and thermodynamics of the air. Perturbations to the stratified atmosphere can cause the generation and propagation of internal waves. In situations where the background density of the fluid does not change significantly over the vertical extent of wave propagation, a simplification known as the Boussinesq approximation is made to the momentum equations. In the momentum equations, density is taken to be constant except when multiplied by gravity in the buoyancy term. This is a commonly used approximation when dealing with internal waves in the stratified ocean where the fluid is nearly incompressible.

The incompressible assumption is not valid for the atmosphere nor can the assumption be made that background density changes are insignificant for waves that propagate over vast vertical distances. Hence, the anelastic approximation, which retains the density profile as a function of height, of the momentum equations is used. As a consequence of conservation of momentum, the amplitudes of upward-propagating anelastic waves will increase as they move into a lower density background. Thus it is important to con-

sider large-amplitude and consequential non-linear effects of waves propagating in an anelastic medium.

Internal waves that propagate through a realistic atmosphere do not encounter a homogeneous background. Background winds can greatly affect internal wave propagation - especially when considering propagation through multiple layers of the atmosphere. When the wind is oriented opposite of the waves' horizontal phase speed, the waves may reflect (a linear theory prediction). However, it is well known that when internal waves reach sufficiently large amplitude, the mean flow induced by the wavepackets may become great enough to counteract a background wind, thus allowing the waves to propagate much higher than predicted by linear theory (Sutherland (2000)). Thus waves may reflect, carrying their momentum back toward the ground, they may transmit past a reflection level and deposit momentum where their amplitudes grow so large that the waves break, or the wavepacket may split where a portion reflects and the rest transmits.

Knowing the location of momentum deposition is imperative for accurately modeling atmosphere dynamics on a large scale. While the magnitude of momentum transport due to internal waves is not precisely known, it is suggested, according to linear theory, that these waves, and the momentum associated with wave breaking or absorption, can substantially alter large-scale mean flow (Booker & Bretherton (1967)). Unfortunately, internal waves have length scales far smaller than the resolution of most general circulation models making the resolution of these waves impractical. The standard solution to this problem is to parameterize internal wave propagation and breaking in the atmosphere using the waves initial parameters to estimate where momentum will be deposited.

The intent of this research is to provide an argument for con-

sidering nonlinear effects of internal waves when they encounter a region of retrograde shear. It will become apparent that using linear theory to approximate the reflection height of large-amplitude waves provides an incomplete picture of actual wave dynamics.

1.1 Motivation

While waves exist in the atmosphere at a variety of length scales, it was originally thought that only planetary-scale waves (10,000 to 40,000km wavelength) had any significant effect on driving mean flows in the middle atmosphere (Holton & Lindzen (1972)). However, it was quickly discovered that these large-scale waves were unable to provide sufficient momentum to drive the mean flows they were thought to be causing (Lindzen (1967); Andrews & McIntyre (1976); Palmer *et al.* (1986); McFarlane (1987)). Dunkerton (1981) found that this momentum deficit was well accounted for when high-frequency Kelvin waves and internal gravity waves were included in a simplified mean-flow interaction model at a wave flux of 2-4 times that of larger-scale Rossby waves. Since then, internal gravity wave dynamics, especially the transport of momentum associated with wave propagation and breaking, in the atmosphere are considered when calculating mean flows in the atmosphere.

Internal waves in the atmosphere can be created by flow over topography, convective storms, and frontal instabilities (Sutherland (2010)). These waves can have an appreciable impact on momentum exchange through vertical layers of the atmosphere (McFarlane (1987)). Since the location of momentum deposition is dependent on where the waves break rather than where they are generated, atmospheric flow over topography has non-localized effects on the mean flow of upper atmosphere layers. Thus, when including these

dynamics in a general circulation model, it is important to understand the dynamics of wave propagation as well as wave generation. Unfortunately, it is computationally prohibitive to resolve internal wave dynamics in general circulation models due to their small length scales, often on the order of kilometers to tens of kilometers (Hamilton (1996); McLandress (1998); Palmer *et al.* (1986); McFarlane (1987)).

As a method to include internal waves without resolving their dynamics, the momentum transport and drag associated with internal waves are parameterized in General Circulation Models (GCMs). In part, these gravity wave drag parameterization schemes attempt to capture momentum deposition due to wave breaking at critical levels. In a shear flow, this is where the horizontal phase speed of the waves matches the background flow speed or, equivalently, where the Doppler-shifted frequency of the waves is zero (Medvedev & Klaassen (1995); Hines (1997); Lindzen (1981); Nastrom & Fritts (1992)). Many of these parameterization schemes ignore much of the complexity of internal wave generation and propagation - including non-linearity and even wave reflection - focusing instead on "launch site" of the waves, linear propagation, and an estimation of location of nonlinear wave overturning (McFarlane (1987)).

Internal wave breaking is the essential final step for internal wave momentum transport. When internal waves break, the turbulence caused by breaking can, itself, excite waves at smaller scales which can, in turn break and create smaller and smaller waves (Lindzen (1981); Staquet & Sommeria (2002)). Eventually the energy cascade leads to waves at such small scales that they dissipate due to viscosity and thermal diffusion (Hamilton (1996)). Concurrently, the wave momentum flux divergence results in momentum that is deposited irreversibly to the background flow providing an acceler-

ation in the direction of the phase speed relative to the background wind (Dunkerton (1981)).

As a result of the decreasing atmosphere density with altitude and of conservation of momentum, the amplitudes of waves grow as they propagate upward, thus providing another mechanism for wave breaking. The gravity wave drag parameterization scheme proposed by Lindzen (1981) used linear anelastic theory to estimate where wave breaking occurs and, consequently, where momentum is deposited. This scheme has improved the accuracy of GCMs (McLandress (1998); Palmer *et al.* (1986); McFarlane (1987)). Wave breaking, however, is an inherently nonlinear process and so the accuracy of linear theory to predict momentum deposition due to anelastic growth and breaking is questionable.

Sutherland (2006) developed a weakly nonlinear theory of Boussinesq internal waves which, through comparison with fully nonlinear simulations, was shown accurately to model the evolution of large-amplitude waves (Sutherland (2006)). The onset of nonlinear dynamics was shown to result from "self-acceleration," in which the wavepacket established a wave-induced mean flow which, in turn, altered the structure of the wavepacket (Fritts & Dunkerton (1984); Sutherland (2001)). Even without the presence of a background flow, the wave-induced mean flow (analogous to the Stokes drift for surface waves) acted to Doppler-shift the frequency of an internal wavepacket - a significant effect for sufficiently large-amplitude waves. In particular, it was observed that when the vertical wavenumber, m, was sufficiently small relative to the horizontal wavenumber, k (specifically $|m/k| < 2^{-1/2}$) the vertical structure of the wavepacket envelope narrowed and steepened through modulational instability. For wavepackets containing larger vertical wavenumber waves, the envelope broadened faster than pre-

dicted by linear dispersion through modulational stability (Sutherland (2006)).

The Boussinesq study was followed by the development of weakly nonlinear theory for internal waves in a non-Boussinesq liquid (Dosser & Sutherland (2011*b*)) and in an anelastic gas (Dosser & Sutherland (2011*a*)). Consistent with Boussinesq theory, anelastic waves were found to be either modulationally stable at high vertical wavenumbers or unstable at low vertical wavenumbers, with marginal stability occurring for waves propagating at the fastest vertical group velocity (Dosser & Sutherland (2011*a*)).

The weakly nonlinear effects of modulational stability and instability were shown to change the height of overturning significantly when compared with linear theory predictions (Dosser & Sutherland (2011*a*)): modulationally unstable wavepackets, which narrow and peak, overturned well below the breaking level predicted by linear theory; modulationally stable wavepackets, which broaden quickly, overturned well above the breaking level predicted by linear theory. In some cases, the difference of observed and linear-theory predicted breaking heights was tens of kilometers.

These studies were performed for waves with zero or uniform background wind. There are few studies of large-amplitude internal waves in non-uniform background flows. Sutherland (2000) presented a fully nonlinear numerical study of the evolution of Boussinesq internal waves in a uniform shear flow with uniform stratification (Sutherland (2000); Sutherland & Linden (1999)). The shear flow was oriented with flow speed increasing with height, its direction oriented opposite to the horizontal phase speed of the incident wavepacket. For a rightward, upward-propagating wave, the negative shear was established so that, according to linear theory, at a certain height, wave reflection would occur due to Doppler-

shifting by the background wind. Explicitly, this occurred where the Doppler-shifted wave frequency matched the background buoyancy frequency (Sutherland (2010)).

Consistent with linear theory, small-amplitude waves propagated upward to the reflection level and then propagated downward. However, for moderately large-amplitude waves, significant momentum was found to transmit across the reflection level. This was shown to result from the positive shear associated with the wave-induced mean flow canceling the negative background shear.

Being restricted to the Boussinesq approximation, the study by Sutherland (2000) of moderately large-amplitude waves in retrograde, uniform shear did not allow for anelastic growth as in Dosser and Sutherland (2011*a*), though the latter study did not include shear. As the next step in developing an understanding of momentum transport by atmospheric internal waves, in this study we synthesize Sutherland (2000) and Dosser and Sutherland (2011*a*) to study the evolution and momentum transport by anelastic waves approaching a reflection level in retrograde shear.

Specifically, we assess the proportion of momentum associated with the incident wavepacket that transmits above, reflects from or is deposited moderately below the reflection level. Of particular physical and theoretical interest is the evolution of incident nearly hydrostatic wavepackets. These are modulationally stable and so weakly nonlinear effects should retard the wavepacket growth suggesting substantial reflection according to linear theory. However, when approaching the reflection level the Doppler-shifted wavepacket becomes modulationally unstable, suggesting the possibility of enhanced transmission or overturning. We examine how this behavior changes as it depends upon the predicted height of the reflection level relative to the predicted height at which weakly nonlinear ef-

fects are expected to become important. Work related to this part of this thesis has been published in Physics of Fluids (Eberly & Sutherland (2014)).

Of further interest is the study of nonlinear, anelastic wave interaction with a background where the buoyancy frequency is non-constant. While it is a basic principle of internal waves that waves may not propagate if their extrinsic frequency is larger than the buoyancy frequency of the ambient fluid, observations have been made of waves in the atmosphere which appear to tunnel through low-buoyancy-frequency regions (Snively & Pasko (2003)). In this study, internal waves which originated near the ground were observed in the ionosphere even though such propagation would require traveling through an evanescent region in the mesosphere.

Sutherland and Yewchuk (2004) performed laboratory experiments to examine internal wave propagation through finite-depth regions of zero, low, and large buoyancy frequency. Analytical predictions for wave transmission through these tunneling regions were found to be in agreement with the experimental models. This provided estimates for transmission of waves through a tunneling region based on the depth and magnitude of the buoyancy frequency change as well as the incident wave parameters. Brown *et al.* (2008) analyzed a fully-nonlinear, numerical model of large-amplitude Boussinesq wavepackets as they propagated through a tunneling region. They found that transmission across the evanescent region was enhanced with increased wavepacket amplitude. Nault and Sutherland (2008) further developed the study of wave tunneling comparing nonlinear, anelastic models of small-amplitude waves to predictions made by a Fourier-ray solution for energy loss through a duct.

Another part of the research presented here examines fully non-

linear, anelastic, numerical models of small-amplitude internal waves as they propagate through an evanescent, tunneling region. These numerical results are compared to an analytical solution for wave transmission through an evanescent region.

Chapter 2

Theory

2.1 Governing Equations

For simplicity, we consider an isothermal atmosphere with temperature T_0. From the ideal gas law and hydrostatic balance, the background density, $\bar{\rho}$, and pressure, $\bar{p}$, decrease with height, z, exponentially as

$$\bar{\rho} = \rho_0 \exp(-z/H_\rho), \tag{2.1}$$

and

$$\bar{p} = p_0 \exp(-z/H_\rho), \tag{2.2}$$

where ρ_0 is the reference density, $p_0 = \rho_0 R_a T_0$ is the reference pressure, R_a is the gas constant for air, and H_ρ is the density scale height. In an isothermal atmosphere, the density scale height is

$$H_\rho = \frac{R_a T_0}{g}, \tag{2.3}$$

in which g is gravity. The background potential temperature is

$$\bar{\theta} = \bar{T}(\bar{p}/p_0)^{-\kappa}, \tag{2.4}$$

where $\bar{T}$ is the temperature profile of the atmosphere and $\kappa = 2/7$ for an ideal diatomic gas. For an isothermal atmosphere, as is the assumption made here, the background potential temperature may

be rewritten in terms of the density scale height by using (2.2) and (2.3) as

$$\bar{\theta} = \theta_0 e^{z/H_\theta}, \tag{2.5}$$

where $\theta_0 = T_0$ is the potential temperature at $z = 0$, and

$$H_\theta = \kappa^{-1} H_\rho. \tag{2.6}$$

The stratification of the atmosphere is represented by the squared buoyancy frequency,

$$N^2 \equiv \frac{g}{\bar{\theta}} \frac{d\bar{\theta}}{dz}. \tag{2.7}$$

In particular, in uniform stratification $N^2 = g/H_\theta$ is constant.

2.2 Anelastic Wave Solutions

When viscosity is not considered, the equations of motion for a fully nonlinear anelastic gas are as follows:

$$\frac{Du}{Dt} = -\frac{\partial}{\partial x}\left(\frac{p}{\bar{\rho}}\right) \tag{2.8}$$

$$\frac{Dw}{Dt} = -\frac{\partial}{\partial z}\left(\frac{p}{\bar{\rho}}\right) + \frac{g}{\bar{\theta}}\theta, \tag{2.9}$$

$$\frac{D\theta}{Dt} = -w\frac{d\bar{\theta}}{dz}, \tag{2.10}$$

and the continuity equation under the anelastic approximation is

$$\nabla \cdot (\bar{\rho}\vec{u}) = 0. \tag{2.11}$$

The material derivative seen in (2.8) and (2.10) is $D/Dt = \partial_t + \vec{u} \cdot \nabla$, where $\nabla \equiv (\partial_x, \partial_z)$. In this case, $\vec{u} = (u, w)$ where u and w represent the horizontal and vertical velocity components of the flow, respectively.

It should be noted that the Coriolis force is neglected here. An analysis of the Rossby number confirms that the Coriolis effect has no significant impact on the flow. The Rossby number is defined as

$$Ro = \frac{U}{fL}, \tag{2.12}$$

Where U and L are the velocity and length scales respectively and f is the Coriolis frequency, $f = 2\Omega \sin\varphi$ where Ω is the rotation rate of the Earth and φ is the latitude of interest. Taking the length scale of internal gravity waves in the atmosphere to be on the order of tens of kilometers and the time scale, $T = L/U$, to be on the order of hundreds of seconds (Fleming *et al.* (1988)), we find that the Rossby number is on the order of 10^2 and is sufficiently high that the Coriolis terms may be neglected.

For small-amplitude, linear waves without advection, equations (2.8), (2.9), and (2.10) may be written as,

$$\frac{\partial u}{\partial t} = -\frac{\partial}{\partial x}\left(\frac{p}{\bar{\rho}}\right), \tag{2.13}$$

$$\frac{\partial w}{\partial t} = -\frac{\partial}{\partial z}\left(\frac{p}{\bar{\rho}}\right) + \frac{g}{\bar{\theta}}\theta, \tag{2.14}$$

and

$$\frac{\partial \theta}{\partial t} = -w\frac{d\bar{\theta}}{dz}. \tag{2.15}$$

Using the continuity equation, (2.11), we write $\vec{u}$ in terms of the streamfunction, Ψ, as,

$$\vec{u} = \left(-\frac{1}{\bar{\rho}}\frac{\partial \Psi}{\partial z}, \frac{1}{\bar{\rho}}\frac{\partial \Psi}{\partial x}\right). \tag{2.16}$$

The spanwise vorticity field may be found by $\zeta \equiv \nabla \times \vec{u}$ giving,

$$\frac{\partial \zeta}{\partial t} = -\frac{g}{\bar{\theta}}\frac{\partial \theta}{\partial x}, \tag{2.17}$$

and

$$\zeta = -\frac{1}{\bar{\rho}}\left(\nabla^2\Psi - \frac{1}{\bar{\rho}}\frac{d\bar{\rho}}{dz}\frac{\partial\Psi}{\partial z}\right). \tag{2.18}$$

Defining $H_\rho \equiv \left(-\frac{1}{\bar{\rho}}\frac{d\bar{\rho}}{dz}\right)^{-1}$ simplifies (2.18) to,

$$\zeta = -\frac{1}{\bar{\rho}}\left(\nabla^2\Psi + \frac{1}{H_\rho}\frac{\partial\Psi}{\partial z}\right). \tag{2.19}$$

Equation (2.15) is recast in terms of Ψ,

$$\frac{\partial\theta}{\partial t} = -\frac{1}{\bar{\rho}}\frac{d\bar{\theta}}{dz}\frac{\partial\Psi}{\partial x}. \tag{2.20}$$

By eliminating θ from (2.17), (2.19), and (2.20), a single equation for the mass streamfunction may be written:

$$\frac{\partial^2}{\partial t^2}\left(\nabla^2\Psi\right) + \frac{1}{H_\rho}\frac{\partial^3\Psi}{\partial z\partial t^2} + N^2\frac{\partial^2\Psi}{\partial x^2} = 0, \tag{2.21}$$

where $N^2 = \left(\frac{g}{\bar{\theta}}\frac{d\bar{\theta}}{dz}\right)^{1/2} = \frac{g}{H_\rho} - \left(\frac{g}{c_s}\right)^2$, $c_s = \sqrt{\gamma R_a T}$, $\gamma = 7/5$, R_a is the gas constant for dry air, and T is temperature.

A plane wave solution of the form,

$$\Psi = \frac{1}{2}A_\Psi \exp i(kx + mz - \omega t)\exp\left(z/2H_\rho\right) + c.c., \tag{2.22}$$

is assumed where c.c. is the complex conjugate and ω is the frequency determined by the dispersion relation,

$$\omega^2 = N^2\frac{k^2}{k^2 + m^2 + \frac{1}{4H_\rho^2}}, \tag{2.23}$$

with horizontal and vertical wavenumbers, k and m, respectively.

This shows that anelastic internal waves are propagating only if the intrinsic frequency, ω, is less than N. The vertical group speed, $c_{gz} = \partial\omega/\partial m$, polarization relations, and other properties of small-amplitude anelastic internal waves are summarized in Table 2.1.

Table 2.1: The polarization relations for anelastic waves in a uniformly stratified fluid in terms of the mass streamfunction, Ψ, defined so that $\vec{u} = \frac{1}{\bar{\rho}}\nabla \times (\Psi \hat{y})$. The phase is represented by $\phi = kx + mz - \omega t$ and $K^2 = k^2 + m^2 + 1/(4H_\rho^2)$. Derivatives of the dispersion relation used in the Schrödinger equation are given for anelastic internal waves in a uniformly stratified fluid. The horizontal and vertical wave numbers are k and m respectively.

Field	Relation to $A_{\psi 0}$
$\Psi = Re(\rho_0 A_{\Psi 0} e^{\imath\phi} e^{-z/2H_\rho})$	$A_{\Psi 0}$
$u = Re(A_{u0} e^{\imath\phi} e^{z/2H_\rho})$	$A_{u0} = \left(-\imath m + \frac{1}{2H_\rho}\right) A_{\psi 0}$
$w = Re(A_{w0} e^{\imath\phi} e^{z/2H_\rho})$	$A_{w0} = \imath k A_{\Psi 0}$
$\zeta = Re(A_{\zeta 0} e^{\imath\phi} e^{z/2H_\rho})$	$A_{\zeta 0} = K^2 A_{\Psi 0}$
$\xi = Re(A_{\xi 0} e^{\imath\phi} e^{z/2H_\rho})$	$A_{\xi 0} = -\frac{K}{N} A_{\Psi 0}$
$\theta = Re(A_{\theta 0} e^{\imath\phi} e^{z/2H_\rho})$	$A_{\theta 0} = \bar{\theta}' \frac{K}{N} A_{\Psi 0}$
$\rho = Re(A_{\rho 0} e^{\imath\phi} e^{-z/2H_\rho})$	$A_{\rho 0} = -\frac{\rho_0}{H_\theta} \frac{K}{N} A_{\Psi 0}$
Dispersion relation and m-derivatives	
$\omega = Nk/K$	
$c_{gz} = \omega_m = -Nkm/K^3$	
$\omega_{mm} = -N\left(3m^2 - K^2\right) k/K^5$	

Our study focuses upon the evolution of horizontally periodic, vertically localized, quasi-monochromatic wavepackets whose vertical structure is given in terms of an amplitude envelope, $A(z,t)$. For example using the solution form (2.22), the vertical displacement field is

$$\xi = A_\xi(z,t) e^{i(kx+mz-\omega t)} e^{z/2H_\rho}, \tag{2.24}$$

where the second exponential captures the anelastic growth predicted by linear theory and it is understood that the actual displacement is the real part of the right-hand side of (2.24). The horizontal and vertical velocity fields, u and w respectively, likewise exhibit exponential growth as $\exp(z/2H_\rho)$.

2.3 Momentum Flux and Induced Mean Flow

Because the horizontally averaged vertical flux of horizontal momentum is defined by

$$F_M = \bar{\rho}\langle uw \rangle, \tag{2.25}$$

in which the angle brackets denote horizontal averaging, we see that F_M does not grow exponentially.

Because the waves are horizontally periodic, one can attribute horizontal momentum to the waves (an exception to the "wave momentum myth" paradigm (McIntyre (1981))). Their momentum is $\bar{\rho}U$ in which U is the wave-induced mean flow, given explicitly by

$$U(z,t) \equiv -\langle \xi\zeta \rangle, \tag{2.26}$$

in which ζ is the spanwise vorticity (Sutherland (2001, 2010); Scinocca & Shepherd (1992)). Using the polarization relations in Table 2.1, it can be shown that

$$U = \frac{1}{2} NK|A_\xi|^2 e^{z/H_\rho}, \tag{2.27}$$

in which $K^2 = k^2 + m^2 + 1/\left(4H_\rho^2\right)$. It can also be shown that the momentum flux is related to the momentum by

$$F_M = c_{gz}\left(\bar{\rho}U\right), \tag{2.28}$$

which is analogous to the relationship between energy flux and energy. (This analogy is explained in detail in Fig 3.7 and associated text of Sutherland (2010).)

2.4 Overturning Condition

Waves overturn where stratification becomes locally unstable when total potential temperature gradient is negative:

$$\frac{d\bar{\theta}}{dz} + \frac{\partial\theta}{\partial z} < 0, \tag{2.29}$$

in which θ is the fluctuation potential temperature. For plane, anelastic waves with vertical displacement amplitude $A_{\xi 0}$ at $z = 0$, (2.29) gives the linear theory prediction for the breaking height (Dosser & Sutherland (2011*a*)):

$$z_b = 2H_\rho \ln\left(\frac{1}{|mA_{\xi 0}|}\right). \tag{2.30}$$

This prediction assumes there is no background shear.

2.5 Doppler-Shifting

As a small-amplitude wavepacket moves vertically through a background wind, the extrinsic (Doppler-shifted) frequency, Ω, changes according to

$$\Omega = \omega - \bar{U}k. \tag{2.31}$$

In particular, if $\bar{U}$ decreases with height, the extrinsic frequency increases. Waves reflect where the extrinsic frequency of a wavepacket matches the background buoyancy frequency, N. In the specific case of linearly decreasing background horizontal velocity $\bar{U} = -s_0 z$, in which $-s_0 < 0$ is the constant background shear, linear theory predicts the reflection height is situated at

$$z_r = \frac{N - \omega}{k s_0}. \tag{2.32}$$

Unlike the background flow, $\bar{U}$, the wave-induced mean flow, U, evolves transiently as the wavepacket evolves. Although the Stokes-drift of surface waves is relatively small even for waves near breaking amplitudes, the wave-induced mean flow of the internal waves can be substantial (Sutherland (2001)). For example, using (2.30) in (2.27), the value of U at the breaking height is $(1/2)NK/m^2$. This can exceed the horizontal phase speed of the waves, N/K, and certainly does so for non-hydrostatic waves with $m \approx 0$, which is the

case for waves near the reflection height. In reality, below the breaking height U acts weakly nonlinearly through Doppler-shifting the waves, which in turn changes the structure of U.

2.6 The Nonlinear Schrödinger Equation

These nonlinear feedback effects are well-modeled by the nonlinear Schrödinger equation (NLS) that describes the evolution of the amplitude envelope of anelastic internal gravity waves in zero background wind (Dosser & Sutherland (2011a)):

$$A_t + c_{gz} A_z = \imath \frac{1}{2} \omega_{mm} A_{zz} - \imath k U A, \tag{2.33}$$

in which U is given by (2.27) and, for writing convenience, we have defined $A \equiv A_\xi$ to be the amplitude envelope of the vertical displacement field, as in (2.24). The first term on the right-hand side of (2.33) denotes linear dispersion and the second (nonlinear) term denotes Doppler-shifting by the wave-induced mean flow, given by (2.27), which is strictly positive and proportional to $|A|^2$.

2.7 Modulational Stability

In general, the modulational stability or instability of a wavepacket is assessed by the relative signs of the coefficients of the dispersion and nonlinear terms (Whitham (1974)). Marginal stability occurs if $\omega_{mm} = 0$, corresponding to waves moving with the fastest vertical group velocity. This occurs for vertical wavenumber m_c such that

$$|m_c/k| = 2^{-1/2} \left[1 + \frac{1}{(2kH_\rho)^2} \right]^{1/2}. \tag{2.34}$$

In the special case of $kH_\rho \gg 1$, the relative vertical wavenumber of marginally stable anelastic waves is identical to that for Boussinesq waves (Sutherland (2006)): $|m_c/k| = 1/\sqrt{2}$.

If $m < m_c < 0$ then $\omega_{mm} > 0$ and the wavepacket is modulationally stable. Hence, the wavepacket widens at a rate faster than that due to linear dispersion and anelastic growth of the amplitude is reduced. This is because the wave-induced mean flow Doppler-shifts the waves to larger vertical wavenumbers which move with faster vertical group speed, causing the wavepacket to spread out. For $m_c < m < 0$, $\omega_{mm} < 0$ and the wavepacket is modulationally unstable; the Doppler-shifted waves move with slower vertical group speed where their amplitude is large causing the wavepacket to narrow and steepen.

Dosser & Sutherland (2011*a*) estimated the height, z_Δ, at which the weakly nonlinear effects become sufficiently large for the effects of modulational stability or instability to become non-negligible:

$$z_\Delta = 2H_\rho \ln\left(\frac{1}{A_{\xi 0}K^2}\sqrt{\frac{2\Delta|m|}{\sigma}}\right), \tag{2.35}$$

where $\Delta \approx 1$ represents the magnitude of the ratio of the leading nonlinear term to the advection term in (2.33), and σ is the vertical extent of the wavepacket. In uniform flow, modulationally unstable waves were found to overturn between z_Δ and z_b due to the accentuated amplitude growth. Modulationally stable waves were found to propagate well above z_b because their anelastic growth rate was reduced by the enhanced spreading of the wavepacket. In fact, for larger $|m/k|$, waves were able to propagate many density scale heights above the breaking height predicted by linear theory (Dosser & Sutherland (2011*a*)).

Sutherland (2000) found that when Boussinesq waves approached a reflection level, their amplitude doubled as the incident, upward-propagating waves combined with the reflected, downward-propagating waves. This in turn quadrupled the wave-induced mean flow which caused sufficiently large amplitude waves to be Doppler-shifted to

higher frequencies and thus begin to reflect at heights below z_r. However, as the trailing edge of the wavepacket approached the reflection level the amplitude of the incident and reflected waves decreased causing a shift to lower frequency and thus a portion of the wavepacket transmitted through the reflection level. These transmitted waves eventually either reflected or dissipated at high levels due to continual Doppler-shifting by the background wind. That study provided criteria for when significant transmission would occur. But it did not assess relative transmission and reflection of momentum above and below z_r.

2.8 Anelastic Wave Tunneling

Of further interest is the study of internal wave interactions in non-uniform stratification. Primary research was conducted by applying a buoyancy frequency profile with a zero-stratification region according to

$$N^2(z) = \begin{cases} N_0^2 & |z| > L/2 \\ 0 & |z| \leq L/2 \end{cases} \tag{2.36}$$

where N_0 is a constant buoyancy frequency, $L/2$ is the height above $z = 0$ where N^2 becomes non-zero. Figure 2.1 shows an example of an N^2 wave tunneling region.

We assume that $\Psi = \hat{\Psi}(z) \exp\left[i(kx - \omega t)\right] \exp\left(-z/2H_\rho\right)$ to satisfy Equation (2.21) such that

$$\hat{\Psi}'' + \left(\frac{N(z)^2}{\omega^2} - 1\right) k^2 \hat{\Psi} = 0. \tag{2.37}$$

Solutions to the initial value problem are then assumed to be of the form

$$\Psi(x, z, t) = A_\Psi \exp\left[i(kx + mz - \omega t)\right] \exp\left(-z/2H_\rho\right). \tag{2.38}$$

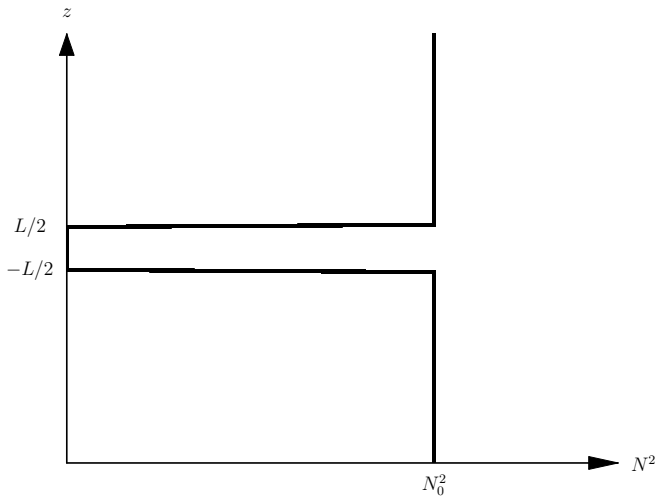

Figure 2.1: A theoretical N^2 tunneling profile where the buoyancy frequency is zero in the region $-L/2 < z < L/2$ and N_0^2 otherwise

where A_Ψ is the mass streamfunction amplitude and ω is given by the dispersion relation

$$\omega^2 = N^2 \frac{k^2}{|K|^2}. \tag{2.39}$$

A piecewise function can be written to represent upward and downward propagating waves below, in, and above the zero stratification region as,

$$\hat{\Psi}(z) = \begin{cases} A_3 \exp(i\gamma z) & z > L/2 \\ A_2 \exp(z/\delta) + B_2 \exp(z/\delta) & L/2 > z > -L/2 \\ A_1 \exp(i\gamma z) + B_1 \exp(-i\gamma z) & z < -L/2. \end{cases} \tag{2.40}$$

where $\gamma = -\left(\frac{N^2k^2}{\omega^2} - k^2 - \frac{1}{4H_\rho^2}\right)^{1/2} = m$, and $\delta = \left(k^2 + \frac{1}{4H_\rho^2}\right)^{-1/2}$. Here, A_1 and B_1, respectively, represent the amplitudes of the upward and downward propagating waves below the tunneling region and A_3 is the amplitude of the upward propagating transmitted wave.

If it is assumed that the piecewise equation must adhere to the interface conditions at $z = \pm L/2$ that $\hat{\Psi}$ must be both continuous

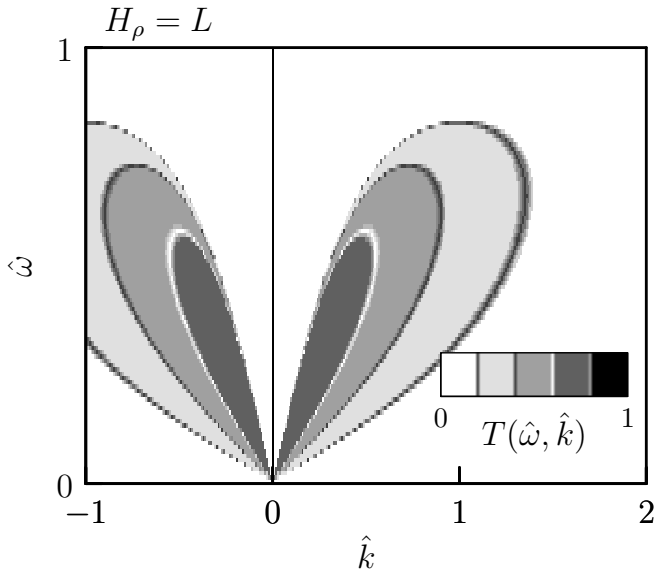

Figure 2.2: Transmission contours, T, as defined in (2.41) for a range of $\hat{k} = kL$ and $\hat{\omega} = \omega/N$ are shown. Here, the density scale height, H_ρ is taken to equal the depth of the tunneling region.

and differentiable. Solving the resulting four equations to find A_3 in terms of A_1, a relationship for transmission may be found similar to that found by Sutherland and Yewchuk (2004) for Boussinesq waves:

$$T \equiv \frac{|A_3|^2}{|A_1|^2} = \left[1 + \frac{(\gamma^2\delta^2 + 1)^2}{(2\gamma\delta)^2} \sinh^2(L/\delta)\right]^{-1} \tag{2.41}$$

A graphical representation of Equation (2.41) is shown in Figure 2.2

Chapter 3

Numerical Methods

3.1 Fully Nonlinear Anelastic Code

The equations used in the code were non-dimensionalized by using the time scale, N^{-1}. For all cases, N remained fixed. Likewise, the length scale, k^{-1}, was fixed in all simulations. In what follows, the equations and analyses are given in units of k and N. All simulations were done using a fully nonlinear, 2D, anelastic code that implicitly solved for spanwise vorticity, ζ, and potential temperature, θ. For now excluding viscosity and diffusion, the vorticity equation is (Dosser & Sutherland (2011a))

$$\frac{D\zeta}{Dt} = -\frac{1}{H_\rho} w\zeta - \frac{g}{\bar{\theta}} \frac{\partial \theta}{\partial x}, \tag{3.1}$$

and the internal energy equation is

$$\frac{D\theta}{Dt} = -w \frac{d\bar{\theta}}{dz}. \tag{3.2}$$

Particularly to avoid the exponential growth of small-scale disturbances near the top of the domain, the code solved the equations of motion written in terms of variables that filtered out the anelastic growth predicted by linear theory. For example, the anelastic-filtered ("hatted") variables representing spanwise vorticity, vertical

displacement, and horizontal and vertical velocity are given implicitly by $(\zeta, \xi, u, w) = (\hat{\zeta}, \hat{\xi}, \hat{u}, \hat{w})e^{z/2H_\rho}$. The details of the transformation of (3.1) and (3.2) to anelastic-filtered variables are provided in Appendix A.

Thus, with the inclusion of diffusion terms, (3.1) and (3.2) are

$$\frac{\partial}{\partial t}\hat{\zeta} = -\bar{U}\hat{\zeta}_x + e^{z/2H_\rho}\left[-\hat{u}\hat{\zeta}_x - \hat{w}\hat{\zeta}_z - \frac{3}{2H_\rho}\hat{w}\hat{\zeta}\right] + N^2\hat{\xi}_x + C_\zeta\nabla^2\hat{\zeta}, \tag{3.3}$$

$$\frac{\partial}{\partial t}\hat{\xi} = -\bar{U}\hat{\xi}_x + e^{z/2H_\rho}\left[-\hat{u}\hat{\xi}_x - \hat{w}\hat{\xi}_z - \left(\frac{1}{2H_\rho} + \frac{1}{H_\theta}\right)\hat{w}\hat{\xi}\right] + \hat{w} + C_\theta\nabla^2\hat{\xi}, \tag{3.4}$$

in which the advective terms of the material derivative, including the background mean flow, have been put on the right-hand side of the equations. Diffusion terms are included in Equations (3.3) and (3.4) for numerical stability but are not intended to accurately reflect the physics of viscous diffusion of waves in the atmosphere. Also, (3.2) has been recast in terms of the approximate vertical displacement using $\xi \equiv -\theta/(d\bar{\theta}/dz)$. The anelastic-filtered mass streamfunction, $\hat{\psi}$, is implicitly related to vorticity using (A.3) and (A.11) to give

$$\hat{\zeta} = -\nabla^2\hat{\psi} + \frac{1}{4H_\rho^2}\hat{\psi}. \tag{3.5}$$

This is inverted to find $\hat{\psi}$ for given $\hat{\zeta}$. The anelastic-filtered velocities are found from (A.1) and (A.2):

$$\hat{u} = -\frac{\partial\hat{\psi}}{\partial z} + \frac{1}{2H_\rho}\hat{\psi}, \tag{3.6}$$

$$\hat{w} = \frac{\partial\hat{\psi}}{\partial x}. \tag{3.7}$$

In order to ensure numerical stability, but not at the expense of excessive wave damping, the coefficients C_ζ and C_θ of the dissipation

terms $C_\zeta \nabla^2 \hat{\zeta}$ and $C_\theta \nabla^2 \hat{\xi}$ were chosen to be zero throughout the domain for waves with horizontal wavenumber less than $0.06k$ as waves at these wavenumbers would be the result of wave breaking and would not significantly affect wavepacket propagation. For larger horizontal wavenumbers, $C_\zeta = C_\theta = 10^{-4} N/k^2$ throughout most of the domain. Hence, small-scale noise was sufficiently damped throughout wave propagation and breaking. To inhibit downward propagating disturbances from the top of the domain, C_ζ and C_θ were enhanced over the top 20% of the domain. This also acted as a sponge layer to damp out noise that tended to grow more rapidly where the background density was small. From the bottom of the sponge layer to the upper bound of the domain, viscosity linearly increased a hundredfold from its background viscosity. Equations (3.3) and (3.4) were solved using a mixed spectral, finite-difference scheme. The code advanced in time by a leap-frog method with Euler back-steps performed every 20 time steps (Sutherland & Peltier (1994)) to minimize splitting errors. This is done by averaging the current fields with the fields from the previous timestep.

The vertical extent of the domain ranged from $z = -30k^{-1}$ to between $120k^{-1}$ and $300k^{-1}$ with larger values chosen in simulations with greater expected height of wave reflection. This ensured that the wavepacket remained far from both boundaries during its evolution. Free-slip boundary conditions were used on both the top and bottom of the domain. The domain was resolved with a vertical grid spacing of $\Delta z = 0.02k^{-1}$. Horizontally, the domain was periodic and set to resolve wavenumbers up to $16k$. Doubling the vertical spatial and horizontal wavenumber resolution had no significant effect on the observed wave dynamics.

The code was initialized with constant background stratification, exponentially decreasing background density $\bar{\rho} = \rho_0 e^{-z/H_\rho}$, and uni-

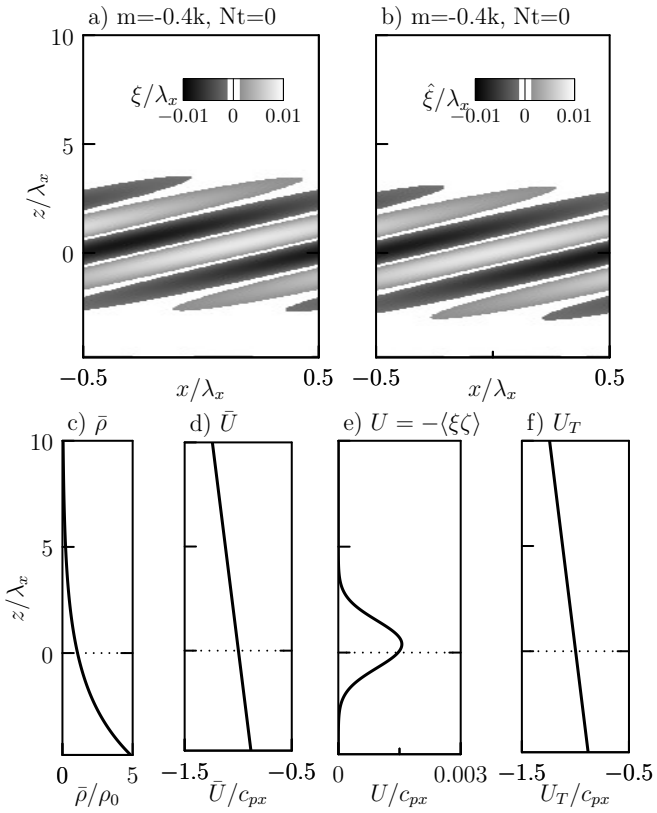

Figure 3.1: Both a) and b) show a snapshot of anelastic waves for $m = -0.4k$, $z_r = H_\rho$ waves at $Nt = 0$. The displacement field, ξ is given in a) and the density-scaled displacement field, $\hat{\xi}$, is shown in b). Figure c) shows an example background density profile, $\bar{\rho}$ and d) a background velocity profile, $\bar{U}$. The wave-induced mean flow is shown in e) and the superposition of d) and e), giving U_T, is shown in f).

form background shear $\bar{U} = U_0 - s_0 z$ with U_0 and s_0 constant, as described below. Additionally, simulations were conducted with a range of background density scale heights ranging from $H_\rho = 10k^{-1}$ to $30k^{-1}$. Most simulations examined the case with $kH_\rho = 20$, corresponding to mesoscale atmospheric internal waves with a horizontal wavelength of approximately 2.5km.

Superimposed on this background was an anelastic, horizontally periodic, vertically Gaussian, quasi-monochromatic wavepacket centered at $z = 0$. The amplitude envelope was initialized according

to

$$\hat{\xi}(x,z,0) = \frac{1}{2}A_0 \exp\left(-z^2/2\sigma^2\right) e^{i(kx+mz)} + c.c., \qquad (3.8)$$

in which *c.c.* denotes the complex conjugate. The vertical extent of the wavepacket was $\sigma = 10k^{-1}$ which ensured the wavepacket was quasi-monochromatic. The initial wavepacket was set to have amplitude $A_0 = 0.05k^{-1}$, which was small enough that the polarization relations of linear theory could be applied to initialize the other fields and was large enough that weakly nonlinear effects were expected to develop shortly after the wavepacket began to move upward and grow anelastically. Making use of the polarization relations (Table 2.1), the initial anelastic-filtered vorticity was given as in (3.8) but with A_0 replaced by $-NKA_0$. Even at the initial time step, there was some flow induced by the waves themselves, $U = -\langle\xi\zeta\rangle$. However, it was small. The background flow at $z = 0$ was set to be $U_0 = -c_{px}$ where $c_{px} = \omega/k$ represents the initial intrinsic horizontal phase speed of the waves. This ensured that while the waves had small amplitude, their horizontal phase did not change in time, which helped to visualize Doppler-shifting effects particularly when examining movies of the simulations.

An example of the initial state is shown in Figure 3.1. The displacement field, ξ, is shown in a). Although these waves are vertically confined to less than one density scale height, it is evident that the anelastic-filtered $\hat{\xi}$ field in b) has smaller amplitude at the leading edge of the wavepacket due to the smaller background density. Likewise, $\hat{\xi}$ is larger than ξ at the trailing edge. This difference between ξ and $\hat{\xi}$ became more obvious when waves propagated upward over many density scale heights such that $\|\xi\|$ grew exponentially and $\left\|\hat{\xi}\right\|$ remained constant until weakly nonlinear effects became important.

Figure 3.1c) shows a typical background density profile and d)

shows the background wind for a case where reflection occurs at $z_r = H_\rho$. Figure 3.1e) shows the initial wave-induced mean flow, $U = -\langle \xi\zeta \rangle$. The total flow, $U_T = \bar{U} + U$, is the superposition of the wave-induced mean flow and the background shear, as shown in Figure 3.1 f). The addition of U to $\bar{U}$ is barely distinguishable from $\bar{U}$ alone (see Figure 3.1d), consistent with the condition that the initial wavepacket had small-amplitude.

In an effort to investigate the behavior of modulationally stable, marginally stable, and modulationally unstable waves, our simulations focused primarily upon a range of wavepackets that had initial wavenumbers of $m = -1.4k$, $-0.7k$, and $-0.4k$ respectively. Waves were allowed to propagate to various reflection heights ranging from $z_r = H_\rho$ to $z_r = 8H_\rho$, as set by the value of the background shear through (2.32). The initial vertical extent of the wavepacket was also varied to ensure the wavepacket was initially quasi-monochromatic. In most cases $\sigma = 10k^{-1}$, but we also set $\sigma = 3k^{-1}$ in large $|m/k|$ simulations.

The simulation run time was estimated from the reflection height and the vertical group speed, c_{gz}. The time for the wavepacket to reach the reflection level was roughly estimated using $t_r = z_r/c_{gz}$ and simulations were run up to time $4t_r$. Time steps of $\Delta t = 0.005N^{-1}$ were used.

The profile of horizontal momentum associated with the waves was calculated by multiplying the difference of the total and background horizontal mean flow by the background density. We denote the result by $\bar{\rho}\langle u \rangle \equiv \bar{\rho}(U_T - \bar{U})$. Consistent with Dosser & Sutherland (2011*a*), we confirmed that the horizontally averaged flow, $\langle u \rangle$, equals the predicted wave-induced mean flow, $U = -\langle \xi\zeta \rangle$ for all z and t up to the point of wave dissipation. When the waves grew so large that they dissipated, the associated momentum became

irreversibly deposited to the background.

3.2 Momentum Quantification

Whether or not the waves dissipated, the total momentum

$$M_T = \int_{z_{min}}^{z_{max}} \bar{\rho}\langle u\rangle dz, \tag{3.9}$$

was conserved.

This fact was used to measure the transmission, reflection, and deposition of momentum by waves in retrograde shear. We define the vertically integrated momentum in the upper, middle and lower parts of the domain by

$$M_U = \int_{z_r}^{z_{max}} \bar{\rho}\langle u\rangle dz, \tag{3.10}$$

$$M_M = \int_{H_\rho}^{z_r} \bar{\rho}\langle u\rangle dz \tag{3.11}$$

and

$$M_L = \int_{z_{min}}^{H_\rho} \bar{\rho}\langle u\rangle dz, \tag{3.12}$$

respectively.

Here, the lower bound of the upper region is z_r (the linear-theory predicted reflection height) and the upper bound of the lower region is H_ρ, one density scale height above $z = 0$. The upper bound of the lower region was chosen to ensure that nearly all the momentum associated with the initial wavepacket was contained in the lower region at initial times and that the waves were able to propagate back into this region at late times. The transmission, reflection, and dissipation of waves were assessed by evaluating M_T, M_U, M_M and M_L at late times in simulations when they were found to be

near steady state. It was found that $t_{max} = 4t_r$ was a good assumption for the attainment of steady state as measurements of transmission and reflection became constant after $t \simeq 2.5t_r$. These late-time integrated total, upper-region and lower-region momenta are denoted by M_T^∞, M_U^∞, and M_L^∞ respectively. The transmission of waves across the reflection level is thus defined in terms of the transmission coefficient

$$T \equiv \frac{M_U^\infty}{M_T^\infty}. \tag{3.13}$$

Similarly, the reflection coefficient is defined to be

$$R \equiv \frac{M_L^\infty}{M_T^\infty}. \tag{3.14}$$

The relative deposition of momentum below the reflection level (between the upper and lower regions) is given by

$$1 - (T + R). \tag{3.15}$$

3.3 Wave Tunneling

The wave tunneling simulations were performed using the same basic code as for the wave reflection in retrograde shear study but with the notable difference of a user-input buoyancy frequency profile. These profiles were generated using MatLab as per the specifications shown in Figure 2.1. The code then solved internally for background potential temperature according to the following relation:

$$\bar{\theta} = \theta_0 \exp\left[\int_{z_0}^{z} \frac{1}{g} N^2(z) dz\right], \tag{3.16}$$

where $N^2(z)$ is the user-input buoyancy frequency profile. Due to its negliable change with height, H_ρ was assumed to remain constant with z despite the height dependency of N^2. U was assumed to be identically zero for this preliminary study.

3.3.1 Wave Tunneling Momentum Quantification

Measurements of momentum were taken similarly to the procedure detailed in Section 3.2. However, only total momentum M_{TT} and momentum above the evanescent region M_{UT} was measured:

$$M_{TT} = \int_{z_{min}}^{z_{max}} \bar{\rho}\langle u\rangle dz, \tag{3.17}$$

and

$$M_{UT} = \int_{L/2}^{z_{max}} \bar{\rho}\langle u\rangle dz, \tag{3.18}$$

where L is defined according to (2.36). The transmission coefficient, T_M, based on momentum rather than energy, was found by dividing the late-time integrated upper-region momentum, M_{UT}^{∞}, by the late-time integrated total momentum, M_{TT}^{∞}:

$$T_M \equiv \frac{M_{UT}^{\infty}}{M_{TT}^{\infty}}. \tag{3.19}$$

Chapter 4

Qualitative Results

4.1 Small Amplitude Wave Reflection from Uniform Retrograde Shear

As a test of the code, simulations are run for the case where waves are predicted to reflect at $z_r = H_\rho$. Because the waves propagated only one density scale height before reaching the reflection level, their amplitude is expected to remain sufficiently small that they should evolve according to linear theory.

The results of simulations with $m = -0.4k$, $m = -0.7k$ and $m = -1.4k$ are shown in Figures 4.1, 4.2 and 4.3, respectively. In all cases, $H_\rho = 20k^{-1}$. The initial state for the simulation results in Figure 4.1 are shown in Figure 3.1.

In all cases, z_r (indicated by the dashed line) is below the height, z_Δ given by (2.35), at which weakly nonlinear effects are expected to become significant (dotted line). Because $z_\Delta > z_r$ in all simulations the wavepacket evolution is well-predicted by linear theory.

In the case where $m = -0.4k$ (Fig. 4.1), as the waves approach the reflection level, the phase lines of the vertical displacement field tilt upward (Figure 4.1b), and then tilt downward to the right after reflection (Figure 4.1c). The wave-induced mean flow, U, and the difference of the horizontally averaged flow and the background,

$\langle u \rangle \equiv \langle U_T \rangle - \bar{U}$, is shown to the right of each displacement field plot. Here, U and $\langle u \rangle$ are small compared to c_{px}, indicating that there is insignificant Doppler-shifting of the waves by the wave-induced mean flow. That both curves are close to overlapping initially is consistent with the assertion that $\langle u \rangle$ is well represented by the correlations $U \equiv -\langle \xi\zeta \rangle$. Upon reflection, the profile of $\langle u \rangle$ lies moderately above the profile of U because the wavefield is composed of a superposition of the upward and downward waves. When the waves propagate well below the reflection level for $Nt \gg 200$ (not shown) the curves come close to overlapping once more. Thus negligible momentum is irreversibly lost to the background flow. The discrepancy between the wave-induced mean flow and the horizontally averaged background flow at late times is due to viscosity which, though small, still dissipated the waves to small degree.

For the case where the wavepacket is moving near its fastest vertical group speed and $m = -0.7k$, Figure 4.2, where the dotted line represents z_Δ as in Figure 4.1, similar linear behavior is observed. It can be noted that the time for the wavepacket to reach the reflection level is significantly less than in the previous case where $m = -0.4k$, Fig. 4.1. Finally, when $m = -1.4k$ (Fig. 4.3) the wavepacket again reflects linearly as expected.

4.2 Nonlinear Reflection

If the reflection level is situated above the height at which weakly nonlinear effects become important, the evolution of the wavepackets is qualitatively different. This is illustrated in Figures 4.4, 4.5, and 4.6 which shows the counterpart of the simulations in Figures 4.1, 4.2, and 4.3 but with $z_r = 4H_\rho$. In all simulations, the reflection level is located above z_Δ but below the overturning level

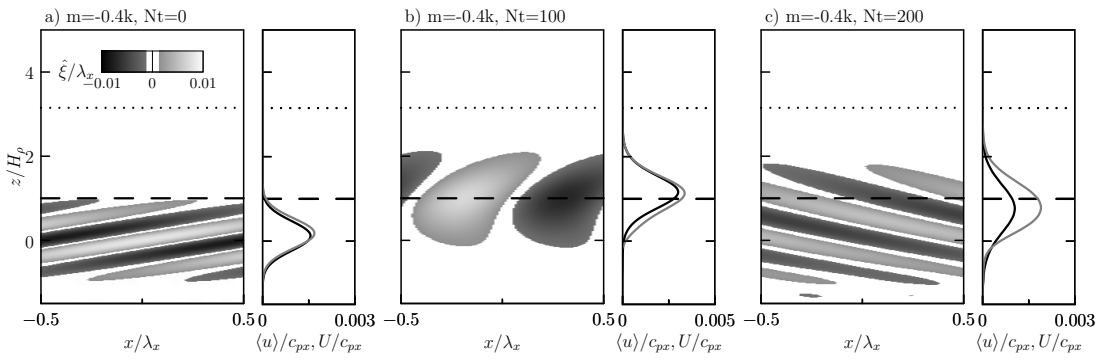

Figure 4.1: Wavepacket evolution in a simulation with $z_r = H_\rho$, $A_0 = 0.05k^{-1}$, and $kH_\rho = 20$ for $m = -0.4k$. Results are shown for three times as indicated. Each plot shows (left) the anelastic-filtered vertical displacement field normalized by horizontal wavelength, $\hat{\xi}/\lambda_x$ (grayscale) and plots (right) of the wave-induced mean flow, U, (black line) compared with the horizontally averaged flow, $\langle u\rangle$ (gray line). The dashed lines indicate the predicted reflection height, z_r, and the dotted lines indicate the height, z_Δ, at which weakly nonlinear effects are expected to become important. Explicitly, $z_\Delta = 3.2H_\rho$. The corresponding overturning height in the absence of shear as predicted by linear theory is (not shown) $z_b = 8.0H_\rho$.

z_b. Explicitly, in Fig. 4.4 for which $m = -0.4k$, $z_\Delta = 3.2H_\rho < z_r = 4H_\rho < z_b = 8.0H_\rho$, in Fig. 4.5 for which $m = -0.7k$, $z_\Delta = 3.2H_\rho < z_r = 4H_\rho < z_b = 6.7H_\rho$ and in Fig. 4.6 for which $m = -1.4k$, $z_\Delta = 2.6H_\rho < z_r = 4H_\rho < z_b = 5.3H_\rho$.

As the wavepacket with $m = -0.4k$ approaches the reflection level (Figure 4.4b), the phase lines tilt somewhat toward the vertical but, because the wavepacket is modulationally unstable, the wavepacket narrows and grows in amplitude. The magnitude of the wave-induced mean flow grows substantially, increasing to $0.16\, c_{px} \simeq 0.15\, N/k$ over a distance of H_ρ. From (2.32), the background shear in this case is $-s_0 = -(N-\omega)/(4kH_\rho) \simeq -0.018N/(kH_\rho)$, which is smaller in magnitude than the characteristic shear, $||dU/dz||$, associated with the wave-induced mean flow. Thus the wave-induced mean flow partially shields the wavepacket from the influence of the background shear, permitting it to propagate above the reflection

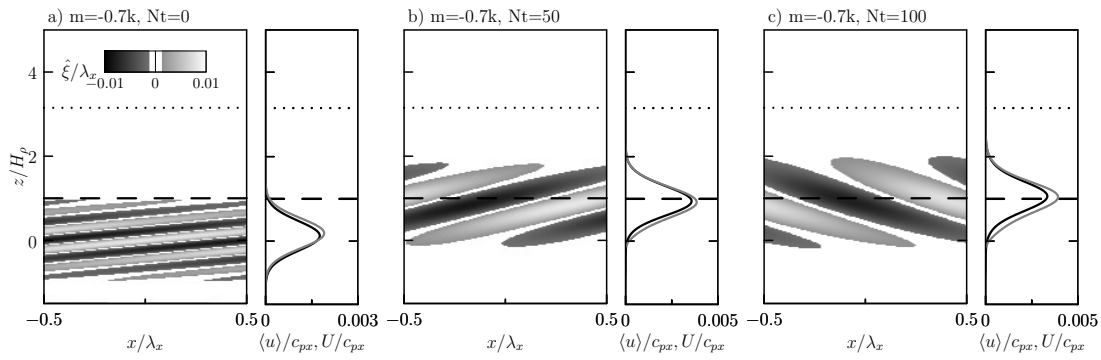

Figure 4.2: Wavepacket evolution in a simulation with $z_r = H_\rho$, $A_0 = 0.05k^{-1}$, and $kH_\rho = 20$ for $m = -0.7k$. Plots and lines indicate the same fields as shown in Figure 4.1. $z_\Delta = 3.2H_\rho$ and $z_b = 6.7H_\rho$.

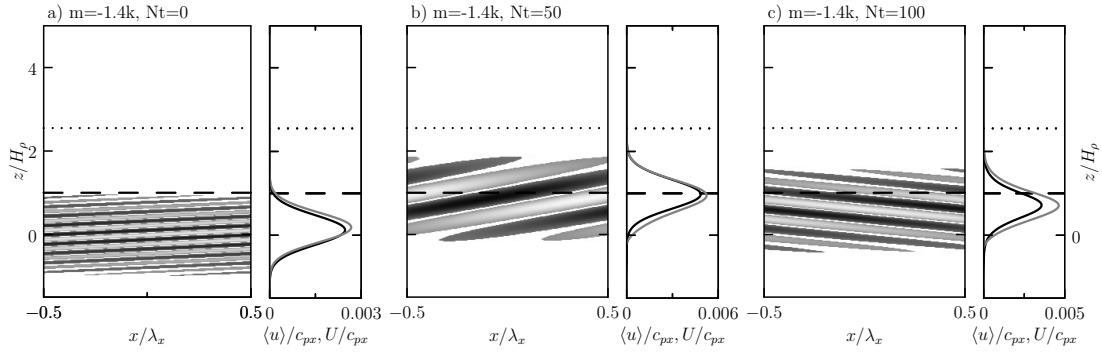

Figure 4.3: Wavepacket evolution in a simulation with $z_r = H_\rho$, $A_0 = 0.05k^{-1}$, and $kH_\rho = 20$ for $m = -1.4k$. Plots and lines indicate the same fields as shown in Figure 4.1. $z_\Delta = 2.6H_\rho$ and $5.5H_\rho$.

level. This becomes clear by time $Nt = 600$ (Figure 4.4c) when a relatively small portion of the wavepacket has reflected but the rest has transmitted across the reflection level. At this time the horizontally averaged flow, $\langle u\rangle$, peaks well above the reflection level with values comparable to c_{px}. U is small compared to $\langle u\rangle$ at this time indicating that the difference in the mean horizontal flow from the background is due to irreversible deposition of momentum from the wave to the background.

The simulation for a marginally stable wavepacket with $m = -0.7k$, and $z_r = 4H_\rho$ is shown in Figure 4.5. Despite the wavepacket's marginal stability, the wave-induced mean flow partially shields

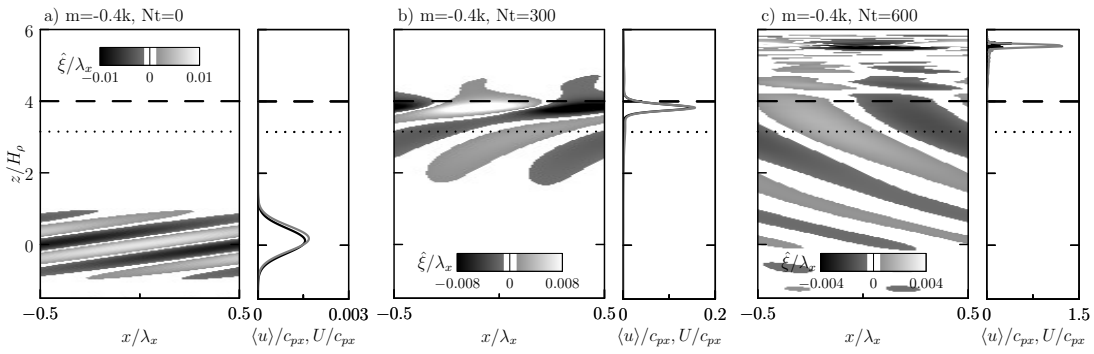

Figure 4.4: As in Fig. 4.1 but for simulations in which the background shear is weaker such that $z_r = 4H_\rho$. The values of z_Δ and z_b are the same as those given in the caption of Fig. 4.1.

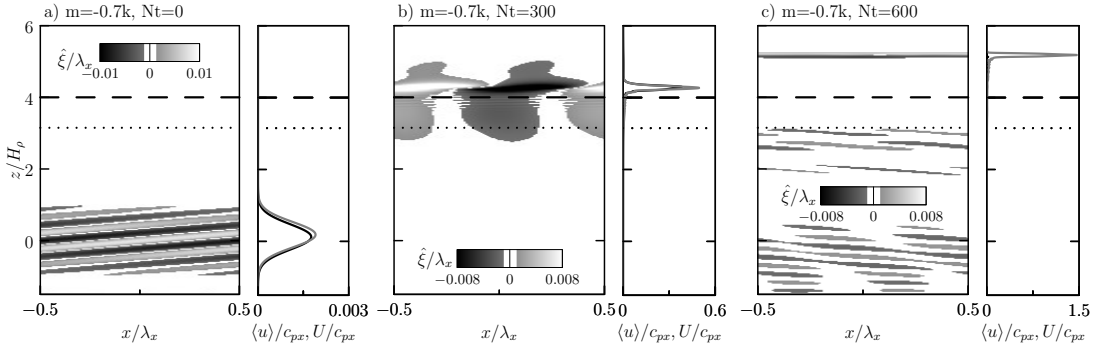

Figure 4.5: As in Fig. 4.2 but for simulations in which the background shear is weaker such that $z_r = 4H_\rho$. The values of z_Δ and z_b are the same as those given in the caption of Fig. 4.2.

the wavepacket from the background flow as in the modulationally unstable case (Fig. 4.4). Here the background shear is $s_0 = 0.0023N/(kH_\rho)$ which is small enough when compared to the characteristic shear that the wavepacket partially transmits and continues to grow to $0.6c_{px}$ at its final breaking point of $4.5H_\rho$.

The corresponding simulation for a modulationally stable wavepacket is shown in Figure 4.6. Even though the amplitude envelopes of modulationally stable wavepackets spread and do not grow as fast as predicted by linear anelastic theory, only a small portion of the wavepacket reflects and undergoes downward propagation. Instead, the shear associated with the wave-induced mean flow peaks

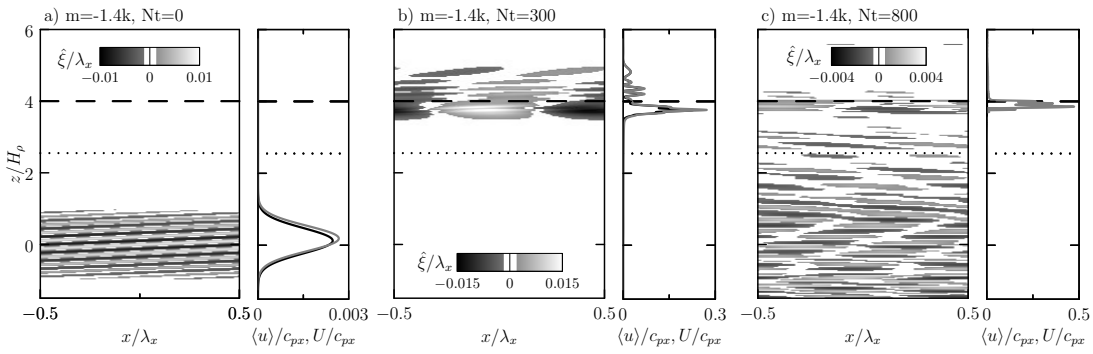

Figure 4.6: As in Fig. 4.3 but for simulations in which the background shear is weaker such that $z_r = 4H_\rho$. The values of z_Δ and z_b are the same as those given in the caption of Fig. 4.3.

just below the reflection level, (Figure 4.6), with a small portion of the wavepacket transmitting and continuing upward propagation. The wave-induced mean flow below z_r at this time peaks at $0.49\, c_{px} \simeq 0.28/\ N/k$, changing over half a density scale height. The shear associated with this is about equal to the background shear of magnitude $s_0 \simeq 0.10N/(kH_\rho)$, but not so large that the wavepacket is shielded from the effects of the background flow as in Fig. 4.4 . Unlike the previous case, the wavepacket does not peak and continue upward propagation. Long after reflection (Figure 4.6c) the majority of the momentum associated with the wavepacket is irreversibly deposited to the background with an increase to the background mean flow just below the reflection level due to the leading portion of the reflected wavepacket combining with the upward-propagating trailing portion. Superpositioning of the wavepacket upon itself leads to a checkerboard pattern but the waves do not exactly cancel. This leads to amplitude growth and wave breaking where the waves superimpose in phase.

The transport and deposition of momentum is clearly illustrated by vertical time series $\langle u\rangle$, as shown in Figure 4.7. Figure 4.7a-c) show three simulations for the case in which $z_r = H_\rho < z_\Delta$ so

that weakly nonlinear effects remain insignificant. In particular, the time series in Figure 4.7a), b), and c) correspond to the simulations shown in Figures 4.1, 4.2 and 4.3, respectively. Figure 4.7d-f) show corresponding time series from simulations with $z_r = 4H_\rho > z_\Delta$, with Figures 4.7d), e) and f) corresponding to the simulations shown in Figures 4.4, 4.5, and 4.6, respectively.

In the simulations with $z = H_\rho$, for which the waves remain small amplitude while reflecting, the mean flow grows as the wavepacket approaches z_r and then returns approximately to its initial value after reflecting and returning to its initial height. Some asymmetry in the mean flow associated with the upward- and downward-propagating wavepacket is observed in the case with $m = -0.4k$ as a result of linear dispersion (Fig. 4.7a): because the vertical extent of the incident wavepacket is $\sigma = 10k^{-1} = 4|m|^{-1}$ the wavepacket is more broad-banded, as compared to simulations with $|m| = 0.7k$ and $1.4k$.

In the three simulations with $z_r = 4H_\rho$, momentum is deposited to the background resulting in irreversible acceleration of the mean flow in each case. In the modulationally unstable case with $m = -0.4k$ (Figure 4.7d), momentum deposition occurs shortly after the wavepacket crosses the reflection level, though still well below the predicted breaking level (at $z_b = 8.0H_\rho$). The acceleration of the background increases as the wavepacket continues to propagate upward into the lower-density background until most of its associated momentum has dissipated. The maximum increase in flow speed occurs near $z = 5.5H_\rho$.

These results differ from those for simulations with $m = -0.4k$ in the Boussinesq study of Sutherland (2000), in which large-amplitude wavepackets deposited their momentum near but below z_r. Here, because the waves grow anelastically, the increasing amplitude of

the disturbance above the reflection level allows for the continual deposition of momentum with consequent increasing mean flow speeds with height.

In the marginally stable case with $m = -0.7k$ (Fig. 4.7e), the evolution of the mean flow is similar to the modulationally unstable case except the height of the maximum mean flow deposition occurs at a moderately lower height, $z \simeq 5H_\rho$. This is to be expected because, as the wavepacket approaches the reflection level, the waves are Doppler-shifted to lower vertical wavenumbers and so become modulationally unstable.

In the modulationally stable case with $m = -1.4k$, both momentum deposition and reflection is evident after propagating above z_Δ and reflecting at z_r, as shown in Figure 4.7f). In this case some background flow acceleration occurs near the reflection level but below the predicted breaking height of $z_b = 5H_\rho$. Even though this wavepacket is modulationally stable, as the wavepacket reflects, the leading edge of the wavepacket is superimposed upon the upward-propagating trailing edge and thus amplitude is doubled at this location. Nonlinear effects are enhanced at the reflection level which drives the wavepacket to breaking amplitudes.

4.3 Wave Tunneling

Simulations were performed for small-amplitude wavepackets where $A_0 = 0.005k^{-1}$ which propagate in a zero-shear, variable background buoyancy frequency according to Equation (2.36) and Figure 2.1 where $H_\rho = 20k^{-1}$ and the evanescent region is either $kL = 0.75$ or $kL = 1.5$.

Figures 4.8, 4.9, and 4.10, display snapshots of these simulations. In all cases, there is at least partial reflection of the wavepacket off

the evanescent or mixed region which is in line with linear theory predictions. Partial transmission of the wavepacket is also seen, to some extent, in each simulation as predicted by (2.41).

Three values of ω were chosen for Figures 4.8, 4.9, and 4.10 with $\omega = 0.5N$, $\omega = 0.75N$, and $\omega = 0.9N$ respectively. The numerical code became unstable for $\omega < 0.5N$ due to small vertical scales and, thus, simulations under such parameters are not discussed here. Additionally, a thin mixed region ($kL = 0.75$) and a wide mixed region ($kL = 1.5$) were considered for each ω given above. In all cases, stratification resumes at a small distance above the mixed region thus ducting theory (Sutherland & Yewchuk (2004)) may be applied.

The wavepackets reflect as they reach the bottom of the mixed region. Also similar to Figure 4.6, wave superpositioning occurs just below the mixed region leading to large increases in both the mean and wave-induced mean flows. After reflection, the portion of the wave packet which was not transmitted across the mixed region propagates downward.

In addition to wave reflection, it is very clear that the wavepacket has partially transmitted through the mixed region. Transmission across the mixed region is seen weakly for Figs. 4.8, 4.9, and 4.10 (a-c) and strongly for Figs. 4.8, 4.9, and 4.10 (d-f) in accordance with "leaky" ducts (Walterscheid *et al.* (2001)). This is a significant observation because more computationally cost effective ray-tracing techniques fail to capture this behavior (Nault & Sutherland (2008)).

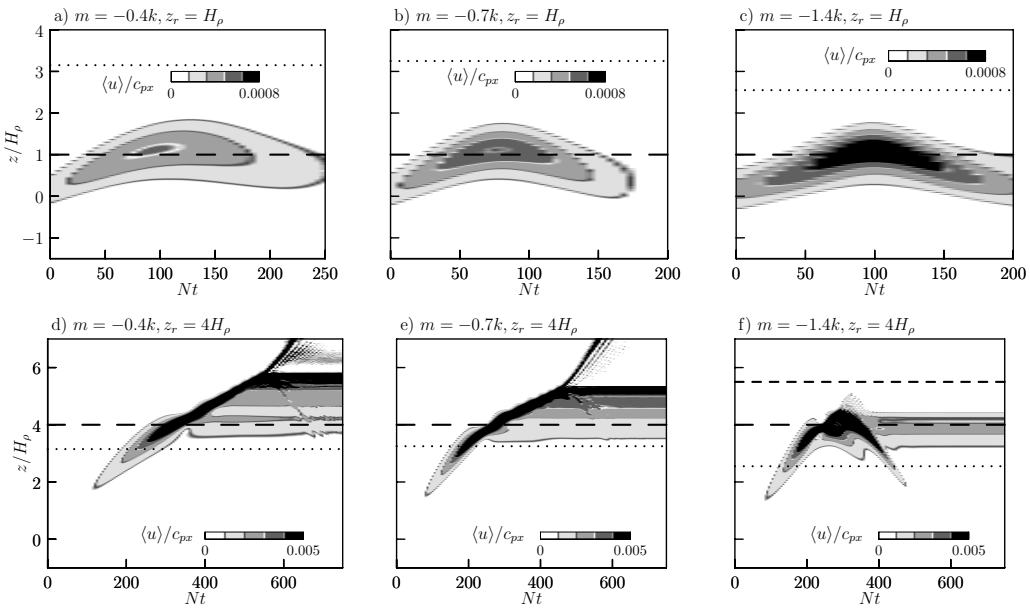

Figure 4.7: Time series of vertical profiles of the normalized mean flow, $\langle u \rangle / c_{px}$ from simulations with $z_r = H_\rho$ and a) $m = -0.4k$, b) $m = -0.7k$ and c) $m = -1.4k$ and with $z_r = 4H_\rho$ and d) $m = -0.4k$, e) $m = -0.7k$ and f) $m = -1.4k$. In all cases $kH_\rho = 20$. Dashed and dotted lines represent the heights, z_r and z_Δ, respectively. The linear theory predicted breaking heights (in the absence of nonuniform shear) are a,d) $z_b = 8.0H_\rho$, b,e) $z_b = 7.0H_\rho$ and c,f) $z_b = 5.5H_\rho$. The breaking level is shown in f) as the short-dashed line.

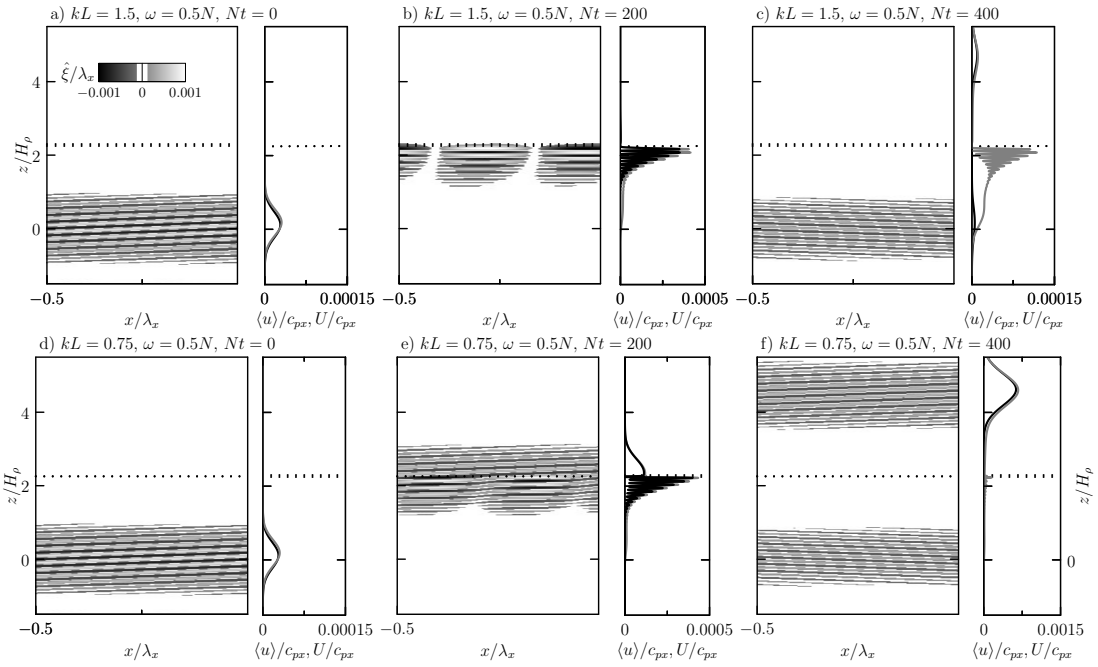

Figure 4.8: Snapshots of wavepacket evolution for a background with $H_\rho = 20$, $s_0 = 0$, $A_0 = 0.005k^{-1}$, and $\omega = 0.5N$. $kL = 1.5$ for the top row and $kL = 0.75$ for the bottom. Dotted lines represent the bottom and top of the $N^2 = 0$ region - the region is thin compared to the vertical extent of the simulation such that the lines appear to overlap. The left panels show the scaled displacement field of the waves while the right plot shows an overlap of the wave-induced mean flow, U in black, and the horizontally averaged mean flow, $\langle u\rangle$ in gray.

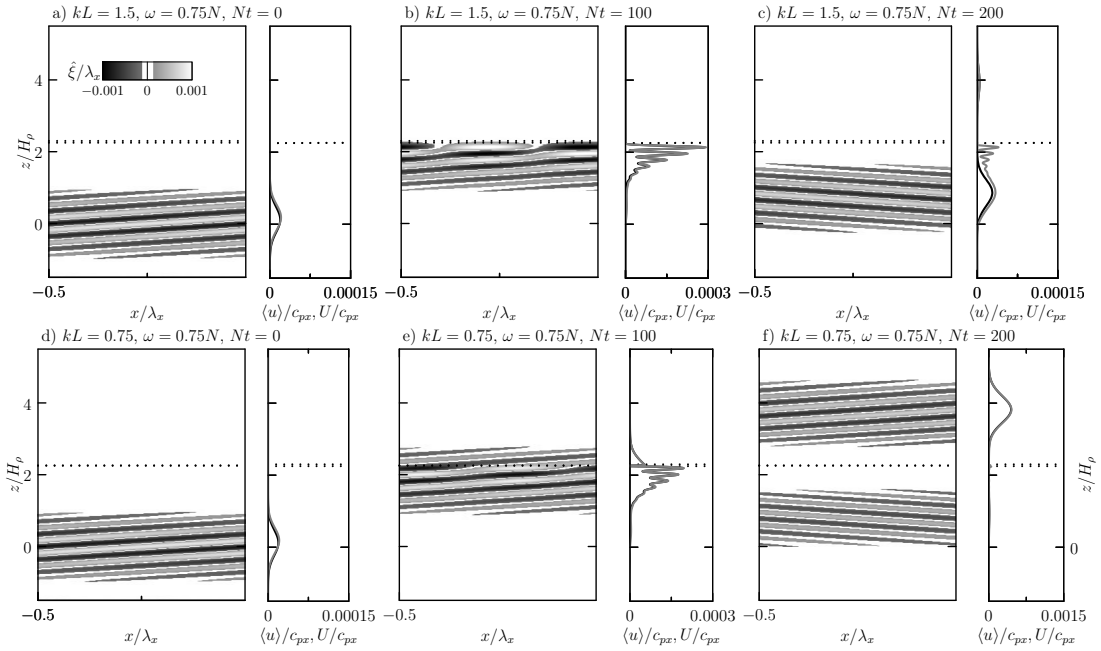

Figure 4.9: As in Figure 4.8 but with $\omega = 0.75N$

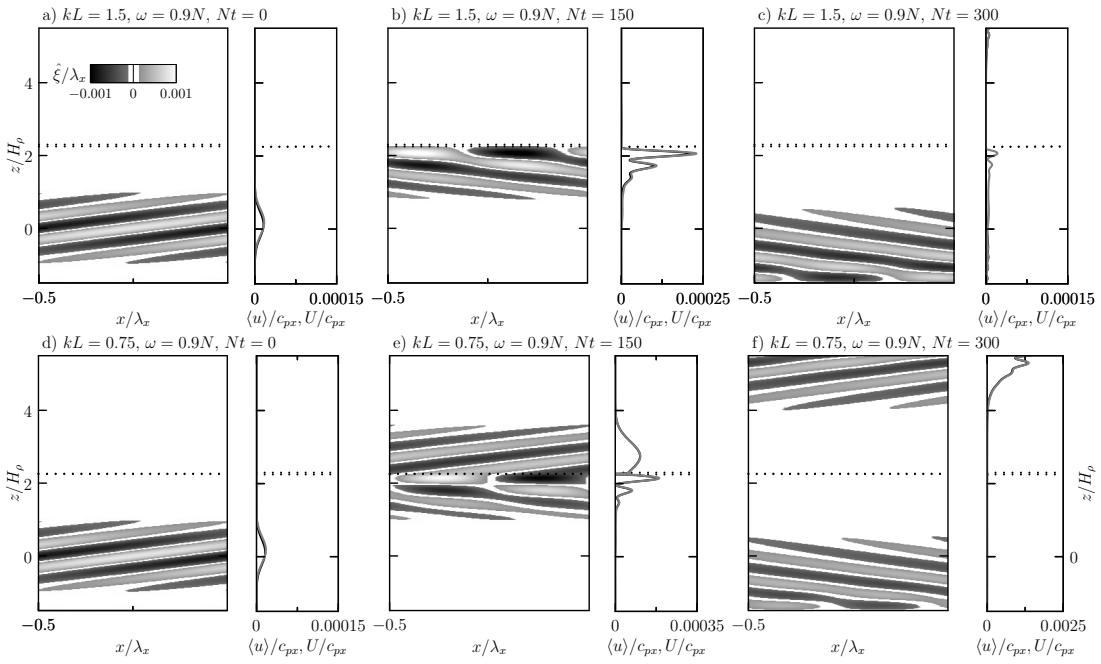

Figure 4.10: As in Figure 4.8 but with $\omega = 0.9N$

Chapter 5

Quantitative Results

5.1 Momentum Calculations for Waves in Retrograde Shear

We crudely characterize the location of momentum deposition in simulations run with wide-ranging parameters by considering the vertically integrated momentum measurements in three domain regions according to (3.9), (3.10), and (3.12). Figure 5.1 shows how these change in time during a simulation in which $H_\rho = 20k$, $m = -1.4k$ and a) $z_r = 2H_\rho$ and $b) z_r = 4H_\rho$. In all cases, $A_0 = 0.05k^{-1}$.

As expected from momentum conservation, M_T (dotted line) remains constant for the duration of the simulations. In both cases, the vertically integrated momentum in the lower domain, M_L (dashed line), is initially equal to M_T because the entire wavepacket is in this region. As time progresses and the wavepacket propagates upward toward the reflection level, momentum leaves the lower domain and M_L decreases while the momentum M_M in the middle region increases.

For the simulation results in Figure 5.1a), the wavepacket reaches the reflection level around $Nt = 100$. At this time, a portion of the wavepacket extends evanescently across the reflection level result-

ing in an increase of the vertically integrated momentum in the upper region, M_U (solid line). During reflection, M_U and M_L do not sum to M_T. The difference is associated with the momentum between the upper and lower regions ($H_\rho \leq z \leq z_r$). After reflection the wavepacket propagates downward into the lower region once more as evident by the increase in M_L and decrease in M_U. After $Nt = 300$, the vertically integrated momenta in each domain have reached steady state with $M_T = M_T^\infty$, $M_L = M_L^\infty$, and $M_U = M_U^\infty$ for the remainder of the simulation. Even after propagating over only two density scale heights, the waves grow sufficiently in amplitude that weakly nonlinear effects became important. The wavepacket mostly reflects (similar to the fully linear simulation with $z_r = H_\rho$, Figure 4.1c). However, at late times some momentum is permanently deposited above the reflection level as indicated by the non-zero value of $M_U^\infty = 0.78 M_T^\infty$. Furthermore, $M_U^\infty + M_L^\infty = 0.84 M_T^\infty$ is less than M_T^∞, indicating that 16% of the total momentum was deposited between $z = H_\rho$ and z_r.

For the results in Figure 5.1b (corresponding to the simulations shown in Figure 4.6 and Figure 4.7f) the wavepacket reflection level is $z_r = 4H_\rho > z_\Delta$, in which case anelastic growth to weakly nonlinear amplitudes is significant before the wavepacket reaches the reflection level. As in Figure 5.1a), when the wavepacket reaches the reflection level, a portion of the wavepacket extends across $z = z_r$. Here, however, the portion of the wavepacket that has crossed the reflection level irreversibly deposits its momentum to the background locally accelerating the background winds. At late times, $M_U^\infty = 0.05 M_T$ is non-zero indicating permanent deposition of momentum above the reflection level. In the lower region, M_L^∞ only reaches 25% of its original value. The non-zero difference, $M_T^\infty - (M_L^\infty + M_U^\infty) = 0.61$ is the fraction of incident momentum irreversibly deposited to the

background flow below the reflection level.

From the values of M_U^∞, M_L^∞, and M_T^∞ determined for a wide range of simulations, we compute the transmission and reflection coefficients using (3.13) and (3.14) respectively. These are plotted in Figure 5.2 along with values of $1-(T+R)$, which is the relative amount of momentum lost to the background between H_ρ and z_r. In all cases where $z_r = H_\rho$, $T \simeq 0$ and $R \simeq 1$. In these low z_r/H_ρ cases, both z_Δ and z_b are significantly higher than the maximum amplitude reached by the wavepacket, as seen in Figures 4.1 and Figures 4.7a-c).

5.2 Transmission and Reflection Coefficients

Figure 5.2a) shows that in weaker shear (so that waves propagate higher before encountering a reflection level and so become increasingly nonlinear due to anelastic growth), less momentum is returned to the lower domain at late times. Instead, the wavepacket either transmits above the reflection level or dissipates between $z = H_\rho$ and z_r. Whether significant transmission above z_r occurs (Figure 5.2b) or momentum is deposited moderately below z_r (Figure 5.2c) depends upon the initial vertical wavenumber, as indicated by the different symbols on each curve.

Of the four relative vertical wavenumbers examined, the steepest decrease in the reflection coefficient with increasing z_r/H_ρ occurs for the modulationally unstable case ($m = -0.4k$), with only a small amount of reflection occurring for $z_r \gtrsim 6H_\rho$. Up to 60% of the momentum is transmitted above the reflection level (for $z_r = 4H_\rho$), but as the shear weakens and z_r increases, the transmission coefficient decreases and most momentum is deposited below the reflection level for $z \gtrsim 6H_\rho$. Similar behavior is observed for the

marginally stable case with $m = -0.7k$.

In the simulations with modulationally stable waves ($m = -1.4k$ and $-3k$), the reflection decreases less rapidly for $m = -1.4k$ and much less rapidly for $m = -3k$. Transmission remains small as z_r/H_ρ increases. The enhanced spreading and relative decrease in the wavepacket amplitude gives a result closer to that predicted by linear theory. The decrease in reflection coefficient with increasing z_r/H_ρ is accounted for by increasing deposition of momentum moderately below z_r. In part this occurs because the breaking level, z_b, predicted by linear theory in the absence of shear also occurs below z_r if $z_r/H_\rho \gtrsim 4H_\rho$. Dosser & Sutherland (2011*a*) showed that weakly nonlinear effects result in modulationally stable wavepackets breaking well above z_b. But this effect combined with wave reflections due to background shear results in momentum deposition and heights near z_r with more reflection and less momentum deposition occurring as $|m/k|$ increases.

5.3 Varying Horizontal Wavelength

Further simulations were also run to examine how the horizontal wavelength relative to density scale height affects transmission in the modulationally stable cases with $m = -1.4k$ and $m = -3k$. In the latter case we set the wavepacket width to be $\sigma = 3k^{-1}$, which still ensures the wavepacket is quasi-monochromatic. kH_ρ ranged from 25 to 3 corresponding to the relative horizontal wavelength, λ_x/H_ρ, ranging from 0.3 to 2.

Figure 5.3 shows the computed reflection and transmission coefficients from simulations with the reflection height fixed at $z_r = 6H_\rho$. Figure 5.3a) shows the reflection and transmission coefficients determined for simulations where $\sigma = 10k^{-1}$ and $m = -1.4k$ (as

indicated by the upward triangles in Figure 5.2 for the specific case with $z_r = 6H_\rho$). As k decreases (λ_x increases) relative to H_ρ, greater reflection but less transmission is observed. For a narrower wavepacket with $\sigma = 3k^{-1}$ and $m = -3k$, similar behavior was observed. In these cases the reflection coefficient is smaller indicating that what does not transmit for the long wavelength cases deposits momentum near the reflection level.

5.4 Wave Tunneling

Momentum transmitted above the evanescent region was measured for the six simulations shown in Figures Figures 4.8, 4.9, and 4.10 according to Equation (3.19). These data were then compared to the analytic prediction for transmission coefficient for anelastic, tunneled waves given in Equation (2.41). This comparison is shown in Figure 5.4

When compared to predictions made by (2.41) measured transmission coefficients (using the momentum-integration method described in Section 3.3.1) were found to be within 2% error of theory. Thus, it is reasonable to conclude that a fully nonlinear anelastic numerical code may accurately predict small-amplitude, tunneling wavepackets.

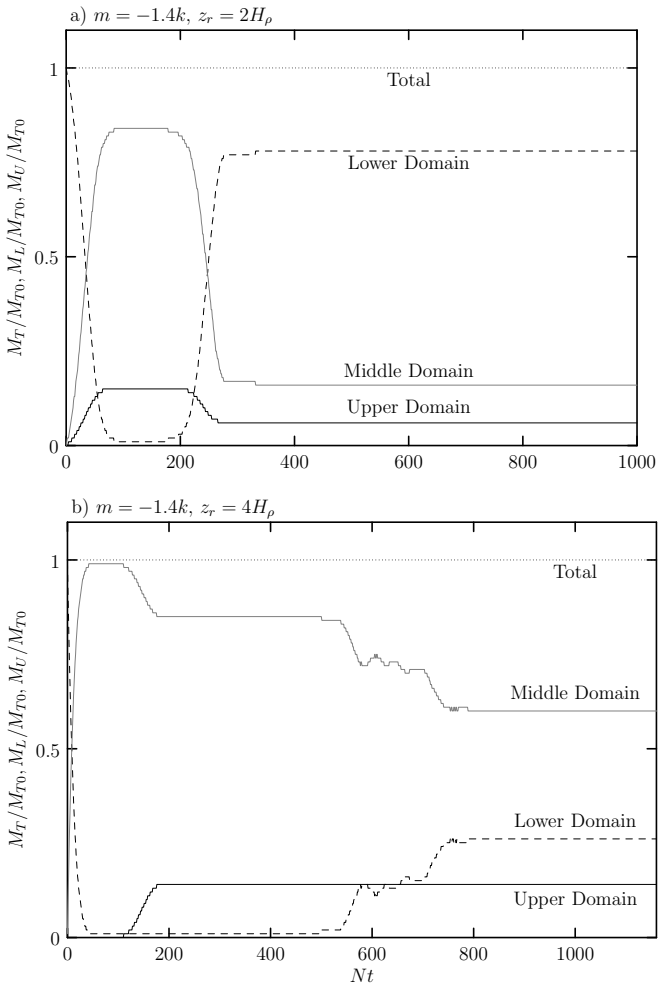

Figure 5.1: Momentum in the whole domain - M_T (dotted), lower domain - M_L (dashed), middle domain - M_M (gray), and upper domain - M_U (solid) related to total momentum at $Nt = 0$, M_{T0}, shown as a function of time for simulations with $kH_\rho = 20$, $m = -1.4k$ and the reflection height at a) $z_r = 2H_\rho$ and b) $z_r = 4H_\rho$.

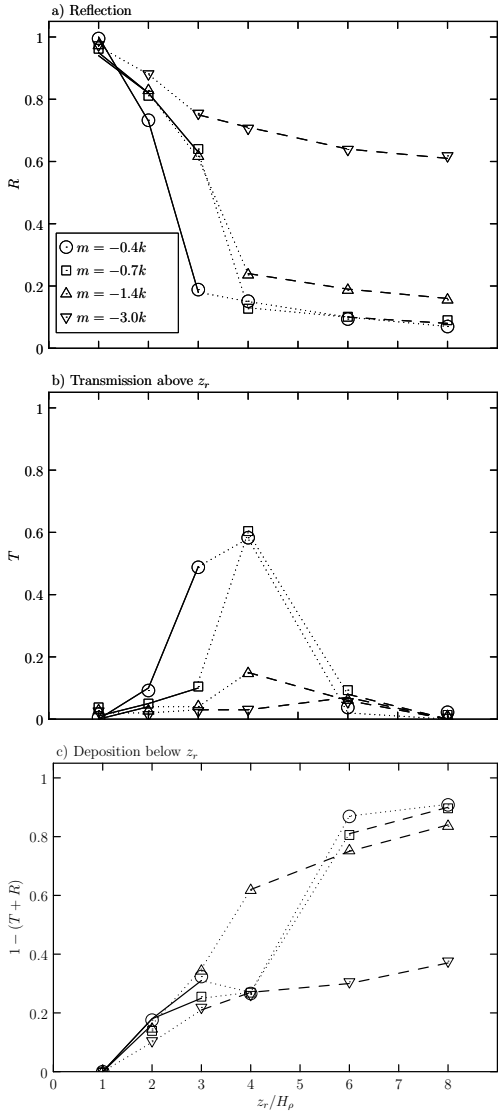

Figure 5.2: Coefficients of a) reflection and b) transmission, and c) the fraction of wave momentum deposited to the background flow for $H_\rho < z < z_r$. In all plots, $kH_\rho = 20$, ($\lambda_x/H_\rho = 0.3$) and $k\sigma = 10$. Solid lines are drawn between the points where $z_r < z_\Delta$, dotted lines are drawn between the points where $z_\Delta < z_r < z_b$, and dashed lines are drawn between the points where $z_r > z_b$. Different symbols are plotted for simulations with different values of m, as indicated in the legend in a).

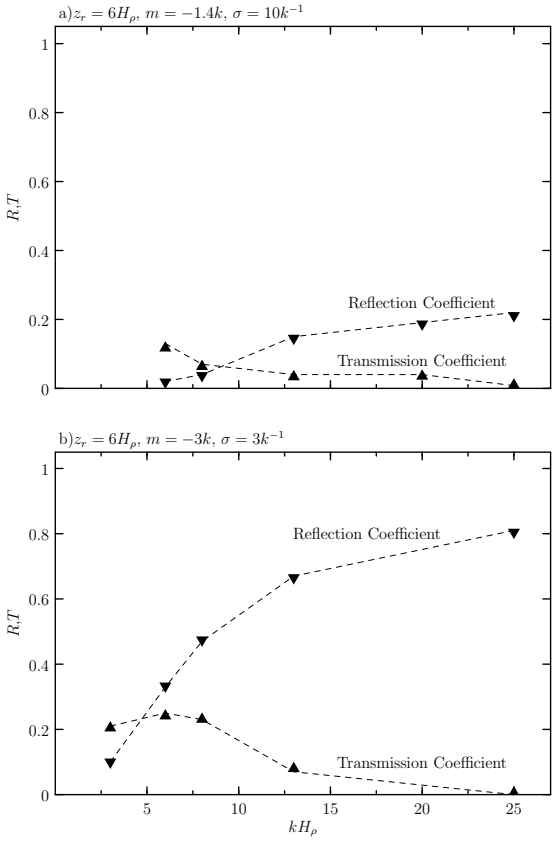

Figure 5.3: Coefficients of reflection (downward triangles) and transmission (upward triangles) as a function of kH_ρ computed from simulations with a) $m = -1.4k$, $\sigma = 10k^{-1}$ and b) $m = -3.0k$, $\sigma = 3k^{-1}$. In all cases $z_r = 6H_\rho$. In a) $z_\Delta \simeq 2.5H_\rho$ and $z_b \simeq 5.3H_\rho$. In b) $z_\Delta \simeq 2.1H_\rho$ and $z_b \simeq 3.8H_\rho$.

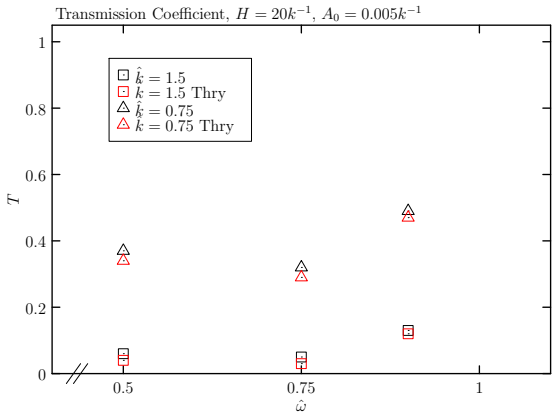

Figure 5.4: Transmission coefficients for measured transmitted momentum, (black markers) and theoretically predicted transmitted momentum (red markers) are given for a range of $\hat{k}$ and $\hat{\omega}$ corresponding to Figures 4.8, 4.9, and 4.10 and Equation (2.41). $\hat{H}_\rho = 1$ and $A_0 = 0.005k^{-1}$.

Chapter 6

Summary and Conclusions

The fully nonlinear anelastic equations were solved to examine the evolution of quasi-monochromatic internal wavepackets in background uniform retrograde shear. If the reflection level was situated at sufficiently low altitude that the wave amplitude remained small as it approached the level, the wavepacket entirely reflected as predicted by linear theory. However, if it was situated above the height, z_Δ, at which weakly nonlinear effects become important, then the wavepacket partially transmitted across the reflection level and some portion of the wavepacket permanently deposited momentum to the background flow below the reflection level. If z_r was well above z_Δ, all momentum for nonhydrostatic waves with $|m| \lesssim 0.7k$ was deposited below z_r even though $z_r < z_b$. When waves are modulationally unstable, the wave-induced mean flow becomes so large that it effectively shields the wavepacket from the effect of the background flow which, in turn, allows a significant portion of the wavepacket to transmit through the reflection level and continue upward propagation until anelastic growth becomes so large that the wave overturns. Conversely, when waves are stable, the wavepacket either reflects linearly (when $z_r < z_\Delta$) or deposits a significant portion of momentum to the background flow just below the reflection level (when $z_\Delta < z_r < z_b$) due to wave superposition. The wave-

induced mean flow, its influence upon the modulational stability of the wavepacket, and its transient modification of the background wind determined the transmission, reflection, and relative momentum deposition coefficients.

Transmission was enhanced for modulationally unstable and marginally stable wavepackets whose amplitude envelope narrowed and grew sufficiently to counteract the Doppler-shifting influence of the background wind. Waves that transmitted continue to be Doppler-shifted and deposited their momentum over a vertical range above z_r. If z_r was very large, though still smaller than z_b, anelastic growth was so significant that waves dissipated before reaching the reflection level.

While Dosser & Sutherland (2011*a*) showed that modulationally stable waves (with large $|m/k|$) broke well above the breaking level predicted by linear theory, this study of waves in retrograde shear showed enhanced reflection and deposition below z_b even if $z_b > z_r$. This was due to transient amplitude growth as the leading, downward-propagating flank of the wavepacket superimposed upon the trailing, upward-propagating flank.

In order to make a more direct comparison between our numerical results and (more significantly energy-containing) atmospheric internal waves, we examined the impact of momentum transmission, reflection and deposition upon increasing relative horizontal wavelength expressed through decreasing kH_ρ. For $kH_\rho \lesssim 6$, corresponding to horizontal wavelengths $\lambda_x \gtrsim 8\,\mathrm{km}$, reflection was negligible with up to 20 % of the momentum transmitting across the reflection level and the remainder being deposited moderately below the reflection level.

At mid-latitudes in the northern hemisphere winter the typical shear and stratification in the stratosphere is $|s_0| \simeq 0.0018 s^{-1}$ and

$N \sim 0.01 s^{-1}$ (Fleming *et al.* (1988)). Taking $H_\rho = 8.4$km and considering a wavepacket with initial vertical displacement amplitude approximately 1% of the horizontal wavelength, corresponding approximations can be made for R and T, and for the altitude, z_d, at which peak acceleration of the background flow occurs due to momentum deposition from either wave superposition or large-scale anelastic growth. These results are given in Table 6.1.

For example, first consider an internal wave with $m = -3k$ ($\omega \simeq 0.003$) at the tropopause. If the horizontal wavelength is $\lambda_x = 25\,\text{km}$, the predicted reflection height is 15 km above. Our simulations show that the entirety of the wavepacket will be reflected back towards the troposphere. Analogous to the simulations shown in Figs. 4.3 and 5.2, the wavepacket in this scenario has not undergone sufficient anelastic growth for nonlinear effects to become significant. Hence it is reasonable to predict that no portion of the wavepacket will transmit above the reflection level.

Next, consider a wavepacket with $m = -1.4k$ and $\lambda_x = 84\,\text{km}$. Here, z_r lies above z_Δ but below z_b - similar to the simulation shown in Fig. 4.6. Anelastic amplitude growth has become significant and nonlinear effects are expected to take hold. As seen in Fig. 4.6, Fig. 6, and Fig. 7, little transmission or reflection is expected - in this case, only 14 % transmission and 20 % reflection. Major momentum deposition is expected to take place just below z_r due to superpositioning of the wavepacket as it undergoes reflection. This can be clearly seen in a similar simulation in Fig. 4.6c). Hence, it would be expected that 66 % of the wave momentum will be deposited 34 km above the tropopause, 20% will be reflected back toward the tropopause and 14% will continue upward propagation toward the stratopause.

Finally, consider a wavepacket with $m = 3k$ and $\lambda_x = 101\,\text{km}$.

In this scenario, $z_b < z_r$ indicating that the wavepacket will become unstable well below the expected reflection height of 62 km. Similar to simulations presented in Fig. 6 where $z_r = 8H_\rho$, it is expected that the wavepacket will become unstable below z_r and momentum deposition will take place near z_b. In this case, it would be expected that the wavepacket will deposit its momentum roughly 32 km above the tropopause with only a small amount (1 %) continuing to propagate upward.

While the reflection of internal waves can well be represented by 2D simulations, wave breaking is an inherently three dimensional phenomenon. However, 2D simulations have been shown to well-capture the wave dynamics even during the early stages of wave breaking (Lund & Fritts (2012)). The results do not attempt to interpret, in detail, the dynamics of wave breaking but rather wave dynamics prior to breaking and consequent momentum deposition.

The buoyancy frequency and shear was uniform for all simulations. However, in the atmosphere, these change dramatically over very large amplitudes. Further research will use a fully nonlinear numerical code to analyze wavepacket interactions in non-uniform background shear and with non-uniform stratification. This research aims ultimately to provide more physically justifiable wave drag parameterization schemes through measurements of momentum deposition heights and strengths determined from fully resolved simulations of propagation and breaking.

Additionally, preliminary predictive equations were derived for transmission of anelastic internal waves through an evanescent or mixed region. When compared to a fully nonlinear model, the measured transmission coefficients were in good agreement with theoretical predictions. Although research of anelastic waves propagating through non-uniform backgrounds is still preliminary, it is hoped

that this research will aid in providing a foundation for fully nonlinear numerical modeling of anelastic waves propagating through realistic atmospheres where both N^2 and $\bar{U}$ are z dependent. Additionally, this may provide a framework for predicting the transmission of internal waves through mixed regions in the atmosphere.

Table 6.1: Predicted reflection height (z_r), predicted breaking height (z_b), predicted height at which nonlinear effects are expected to become significant (z_Δ), estimated height of maximum irreversible mean flow acceleration due to overturning (z_d), estimated reflection coefficient (R), and transmission coefficient (T), given for a range of λ_x and for $m = -1.4k$ and $m = -3k$. Values of R and T are estimated by scaling the results plotted Figures 5.2 and 5.3 to match typical stratospheric conditions in northern hemisphere winter, for which $s_0 = 0.0018\text{s}^{-1}$ and $N = 0.01\text{s}^{-1}$. In all cases the vertical extent of the wavepacket is $\sigma = 3k^{-1}$ and the wave amplitude at the bottom of the stratosphere (taken to be $z = 0$) is $A = 0.05k^{-1} \simeq 1\%\,\lambda_x$. No value of z_d is given if no overturning and hence no irreversible mean flow acceleration occurs.

λ_x (km)	$m = -1.4k$						$m = -3k$					
	z_r (km)	z_b (km)	z_Δ (km)	z_d (km)	R	T	z_r (km)	z_b (km)	z_Δ (km)	z_d (km)	R	T
25	9	45	31		1.0	0.0	15	32	17		1.0	0.0
42	16	45	31	16	0.90	0.01	25	32	17	25	0.78	0.01
59	23	45	30	23	0.61	0.05	36	32	17	32	0.23	0.10
84	35	44	28	34	0.20	0.14	51	32	16	32	0.05	0.03
101	44	44	26	44	0.17	0.05	62	32	16	32	0.0	0.01
118	53	44	26	44	0.05	0.0	73	32	15	32	0.0	0.0

Appendices

Appendix A

Here we derive the formulae for the basic state fields solved by the numerical model. From the anelastic approximation to the continuity equation, $\nabla \cdot (\bar{\rho} u) = 0$, it follows that one can write the velocity components in terms of a mass streamfunction, ψ, according to

$$u = -\frac{1}{\bar{\rho}} \frac{\partial \psi}{\partial z}, \tag{A.1}$$

and

$$w = \frac{1}{\bar{\rho}} \frac{\partial \psi}{\partial x}. \tag{A.2}$$

The spanwise vorticity is

$$\zeta = \frac{\partial u}{\partial z} - \frac{\partial w}{\partial x} = -\frac{1}{\bar{\rho}} \left[\nabla^2 \psi + \frac{1}{H_\rho} \frac{\partial \psi}{\partial z} \right], \tag{A.3}$$

in which $H_\rho = -\left(\frac{\bar{\rho}'}{\bar{\rho}} \right)^{-1}$ is the density scale height.

The fully nonlinear momentum equations for an anelastic gas are

$$\frac{Du}{Dt} = -\frac{\partial}{\partial x} \left(\frac{p}{\bar{\rho}} \right), \tag{A.4}$$

$$\frac{Dw}{Dt} = -\frac{\partial}{\partial z} \left(\frac{p}{\bar{\rho}} \right) + \frac{g}{\bar{\theta}} \theta, \tag{A.5}$$

and

$$\frac{D\theta}{Dt} = -w \frac{d\bar{\theta}}{dz}. \tag{A.6}$$

Taking the curl of the momentum conservation equations, neglecting viscosity, the equation for evolution of vorticity is

$$\frac{D\zeta}{Dt} = -\frac{1}{H_\rho} w\zeta - \frac{g}{\bar{\theta}} \frac{\partial \theta}{\partial x}. \tag{A.7}$$

Neglecting thermal diffusion, the internal energy equation is

$$\frac{D\theta}{Dt} = -w \frac{d\bar{\theta}}{dz}. \tag{A.8}$$

Rather than work with θ, we cast the internal energy equation more intuitively in terms of ξ, defined implicitly by

$$\theta = -\frac{d\bar{\theta}}{dz} \xi. \tag{A.9}$$

The quantity ξ well approximates the vertical displacement field if the displacement is much smaller compared with the potential temperature scale height, H_θ. Likewise, we approximate $d\bar{\theta}/dz$ as locally constant upon substituting (A.9) into (A.8) to give

$$\frac{D\xi}{Dt} = w. \tag{A.10}$$

Due to the exponential decrease of $\bar{\rho}$, the basic state fields are expected to change exponentially at leading order in linear theory. Accounting for this, we work with variables that do not exhibit such exponential changes. These "hatted" variables are defined implicitly by

$$\begin{aligned}
\zeta(x,z,t) &= \hat{\zeta}(x,z,t) e^{z/2H_\rho} \\
\vec{u}(x,z,t) &= \hat{\vec{u}}(x,z,t) e^{z/2H_\rho} \\
\theta(x,z,t) &= \hat{\theta}(x,z,t) e^{z/2H_\rho} e^{z/H_\theta} \\
\psi(x,z,t) &= \hat{\psi}(x,z,t) e^{-z/2H_\rho} \\
\xi(x,z,t) &= \hat{\xi} e^{z/2H_\rho}.
\end{aligned} \tag{A.11}$$

Relationships for the above variables to the streamfunction can be found in Table 2.1.

By applying the scalings in (A.11) to (A.7) and (A.10), the evolution equations for $\hat{\zeta}$ and $\hat{\xi}$ are

$$\frac{\partial \hat{\zeta}}{\partial t} = e^{z/2H_\rho}\left[-\hat{u}\hat{\zeta_x} - \hat{w}\hat{\zeta_z} - \frac{3}{2H_\rho}\hat{w}\hat{\zeta}\right] + N^2\hat{\xi_x}, \tag{A.12}$$

and

$$\frac{\partial \hat{\xi}}{\partial t} = e^{z/2H_\rho}\left[-\hat{u}\hat{\xi_x} - \hat{w}\hat{\xi_z} - \left(\frac{1}{2H_\rho} + \frac{1}{H_\theta}\right)\hat{w}\hat{\xi}\right] + \hat{w}. \tag{A.13}$$

The final step is to include the background flow, $\bar{U}$ in (A.12) and (A.13) giving

$$\frac{\partial}{\partial t}\hat{\zeta} = -\bar{U}\hat{\zeta_x} + e^{z/2H_\rho}\left[-\hat{u}\hat{\zeta_x} - \hat{w}\hat{\zeta_z} - \frac{3}{2H_\rho}\hat{w}\hat{\zeta}\right] + N^2\hat{\xi_x}, \tag{A.14}$$

and

$$\frac{\partial}{\partial t}\hat{\xi} = -\bar{U}\hat{\xi_x} + e^{z/2H_\rho}\left[-\hat{u}\hat{\xi_x} - \hat{w}\hat{\xi_z} - \left(\frac{1}{2H_\rho} + \frac{1}{H_\theta}\right)\hat{w}\hat{\xi}\right] + \hat{w}. \tag{A.15}$$

Including diffusion in (A.14) and (A.15) gives (3.3) and (3.4), which are explicitly solved by the numerical code.

Bibliography

Andrews, D. G. & McIntyre, M. E. 1976 Planetary waves in horizontal and vertical shear: The generalized Eliassen-Palm relation and the mean flow acceleration. *J. Atmos. Sci.* **33**, 2031–2048.

Booker, J. R. & Bretherton, F. P. 1967 The critical layer for internal gravity waves in shear flow. *J. Fluid Mech.* **27**, 513–539.

Brown, G. L., Bush, A. B. G. & Sutherland, B. R. 2008 Beyond ray tracing for internal waves. Part II: Finite-amplitude effects. *Phys. Fluids* **20**, 106602–1–13, doi:10.1063/1.2993168.

Dosser, H. V. & Sutherland, B. R. 2011*a* Anelastic internal wavepacket evolution and stability. *J. Atmos. Sci.* p. in press.

Dosser, H. V. & Sutherland, B. R. 2011*b* Weakly nonlinear non-Boussinesq internal gravity wavepackets. *Physica D* **240**, 346–356.

Dunkerton, T. J. 1981 Wave transience in a compressible atmosphere. Part I: Transient internal wave, mean-flow interaction. *J. Atmos. Sci.* **38**, 281–297.

Eberly, L. E. & Sutherland, B. R. 2014 Anelastic internal wave reflection and transmission in uniform retrograde shear'. *Phys. of Fluids* **26**, 026601.

Fleming, E., Chandra, S., Shoeberl, M. & Barnett, J. 1988 Monthly mean global climatology of temperature, wind, geopotential height, and pressure for 0-120km. *Tech. Rep.* 100697. NASA.

Fritts, D. C. & Dunkerton, T. J. 1984 A quasi-linear study of gravity-wave saturation and self-acceleration. *J. Atmos. Sci.* **41**, 3272–3289.

Hamilton, K. 1996 Comprehensive meteorological modelling of the middle atmosphere: A tutorial review. *J. Atmos. Terres. Phys.* **58**, 1591–1627.

Hines, C. O. 1997 Doppler-spread parameterization of gravity-wave momentum deposition in the middle atmosphere. Part 1: Basic formulation. *J. Atmos. Terr. Phys.* **59**, 371–386.

Holton, J. R. & Lindzen, R. S. 1972 An updated theory for the quasi-biennial cycle of the tropical stratosphere. *J. Atmos. Sci.* **29**, 1076–1080.

Lindzen, R. D. 1967 Planetary waves on beta-planes. *Mon. Wea. Rev.* **95**, 441–451.

Lindzen, R. S. 1981 Turbulence and stress owing to gravity wave and tidal breakdown. *J. Geophys. Res.* **86**, 9707–9714.

Lund, T. & Fritts, D. 2012 Numerical simulation of gravity wave breaking in the lower thermosphere. *J. Geophys. Res.* **117**, D21105.

McFarlane, N. A. 1987 The effect of orographically excited gravity wave drag on the general circulation of the lower stratosphere and troposphere. *J. Atmos. Sci.* **44**, 1775–1800.

McIntyre, M. E. 1981 On the wave momentum myth. *J. Fluid Mech.* **58**, 331–347.

McLandress, C. 1998 On the importance of gravity waves in the middle atmosphere and their parameterization in general circulation models. *J. Atmos. Sol.-Terres. Phys.* **60**, 1357–1383.

Medvedev, A. S. & Klaassen, G. P. 1995 Vertical evolution of gravity wave spectra and the parameterization of associated wave drag. *J. Geophys. Res.* **100**, 25841–25853.

Nastrom, G. D. & Fritts, D. C. 1992 Sources of mesoscale variability of gravity waves. Part I: Topographic excitation. *J. Atmos. Sci.* **49**, 101–110.

Nault, J. T. & Sutherland, B. R. 2008 Beyond ray tracing for internal waves. Part I: Small-amplitude anelastic waves. *Phys. Fluids* **20**, 106601–1–10, doi:10.1063/1.2993167.

Palmer, T. N., Shutts, G. J. & Swinbank, R. 1986 Alleviation of a systematic westerly bias in general circulation and numerical weather prediction models through an orographic gravity drag parametrization. *Quart. J. Roy. Meteor. Soc.* **112**, 1001–1039.

Scinocca, J. F. & Shepherd, T. G. 1992 Nonlinear wave-activity conservation laws and Hamiltonian structure for the two-dimensional anelastic equations. *J. Atmos. Sci.* **49**, 5–27.

Snively, J. B. & Pasko, V. P. 2003 Breaking of thunderstorm-generated gravity waves as a source of short-period ducted waves at mesopause altitudes. *Geophys. Res. Lett.* **30** (24), 2254, doi:10.1029/2003GL018436.

Staquet, C. & Sommeria, J. 2002 Internal gravity waves: From instabilities to turbulence. *Ann. Rev. Fluid Mech.* **34**, 559–593.

Sutherland, B. R. 2000 Internal wave reflection in uniform shear. *Q.J.R.M.S.* **126**, 3255–3287.

Sutherland, B. R. 2001 Finite-amplitude internal wavepacket dispersion and breaking. *J. Fluid Mech.* **429**, 343–380.

Sutherland, B. R. 2006 Weakly nonlinear internal wavepackets. *J. Fluid Mech.* **569**, 249–258.

Sutherland, B. R. 2010 *Internal Gravity Waves*. Cambridge, UK: Cambridge University Press.

Sutherland, B. R. & Linden, P. F. 1999 An experimental/numerical study of internal wave transmission across an evanescent level. In *Mixing and Dispersion in Stably Stratified Flows* (ed. P. A. Davies), pp. 251–262. IMA, Oxford University Press.

Sutherland, B. R. & Peltier, W. R. 1994 Turbulence transition and internal wave generation in density stratified jets. *Phys. Fluids A* **6**, 1267–1284.

Sutherland, B. R. & Yewchuk, K. 2004 Internal wave tunnelling. *J. Fluid Mech.* **511**, 125–134.

Walterscheid, R. L., Schubert, G. & Brinkman, D. G. 2001 Small-scale gravity waves in the upper mesosphere and lower thermosphere generated by deep tropical convection. *J. Geophys. Res.* **106** (D23), 31825–31832.

Whitham, G. B. 1974 *Linear and Nonlinear Waves*. New York, USA: John Wiley and Sons, Inc.